JOURNAL OF PETROLOGY | VOLUME 55 | NUMBER 2 | PAGES 283–313 | 2014 | doi:10.1093/petrology/egt067

The Beni Bousera Peridotite (Rif Belt, Morocco): an Oblique-slip Low-angle Shear Zone Thinning the Subcontinental Mantle Lithosphere

ERWIN C. FRETS[1,2]*, ANDRÉA TOMMASI[2], CARLOS J. GARRIDO[1], ALAIN VAUCHEZ[2], DAVID MAINPRICE[2], KAMAL TARGUISTI[3] AND ISMA AMRI[3]

[1]INSTITUTO ANDALUZ DE CIENCIAS DE LA TIERRA (IACT), CSIC & UGR, AVENIDA DE LAS PALMERAS 4, 18100 ARMILLA, GRANADA, SPAIN

[2]GEOSCIENCES MONTPELLIER, CNRS & UNIVERSITÉ DE MONTPELLIER 2, F-34095 MONTPELLIER CEDEX 5, FRANCE

[3]DÉPARTEMENT DE GÉOLOGIE, FACULTÉ DES SCIENCES, UNIVERSITÉ ABDELMALEK ESSAÂDI, TETOUAN, MOROCCO

RECEIVED AUGUST 7, 2012; ACCEPTED OCTOBER 17, 2013

Detailed structural and petrological mapping in the Beni Bousera peridotite (Rif Belt, northern Morocco) shows that this orogenic peridotite massif is composed of four tectono-metamorphic domains with consistent kinematics, marked by a pervasive, shallowly dipping foliation with a NW–SE stretching lineation that progressively rotates towards a NNE–SSW orientation in the lowermost part of the massif. From top to bottom, these domains are garnet–spinel mylonites, Ariègite subfacies fine-grained porphyroclastic spinel peridotites, Ariègite–Seiland subfacies porphyroclastic, and Seiland subfacies coarse-porphyroclastic to coarse-granular spinel peridotites. Microstructures and crystal preferred orientations point to deformation dominantly by dislocation creep in all domains, but the continuous increase in average olivine grain size indicates decreasing plastic work rates from top to bottom. This evolution in deformation conditions is consistent with the change in synkinematic pressure and temperature conditions, from 900°C at 2·0 GPa in garnet–spinel mylonites to 1150°C at 1·8 GPa in the Seiland domain. A pervasive diffuse dunitic–websteritic layering subparallel to the foliation suggests deformation in the presence of melt in the Seiland domain. Gravitational instabilities owing to local melt accumulation may account for <200 m wide areas exhibiting a vertical lineation in this domain. To account for the consistent kinematics and the tectono-metamorphic evolution, which implies a temperature gradient of c. *125°C km^{-1} preserved across the Beni Bousera massif, we propose that the entire massif records the functioning of a low-angle shear zone, a few kilometres wide, which accommodated exhumation of the base of the lithosphere from ~90 to ~60 km depth. Partial melting in the Seiland domain may be explained by fast decompression of the footwall, without the need for exotic heat sources. Moreover, if the present-day orientation of the shear zone is similar to that when it was active in the mantle, the stretching lineations at high angle to the metamorphic gradient imply that shearing parallel to the trend of the belt accompanied thinning; that is, a transtensional deformation of the margin.*

KEY WORDS: *mantle; continental lithosphere; shear zone; deformation; microstructures; olivine; pyroxenes; crystal preferred orientations; thinning; decompression; belt-parallel flow; transtension*

INTRODUCTION

Extension, leading to thinning of the continental lithosphere, occurs in narrow localized domains forming continental rifts, such as the East African, Baikal and Rio Grande rifts, in a diffuse manner, as in the Basin and Range Province, and in active, previously thickened convergent continental margins, such as the Himalayas and the Alps (e.g. Burchfiel *et al.*, 1992; Sue *et al.*, 1999). However, the processes controlling the thinning of the

*Corresponding author. Present address: Instituto Andaluz de Ciencias de la Tierra (IACT), CSIC & UGR, Avenida de las Palmeras 4, 18100 Armilla, Granada, Spain. E-mail: erwin.frets@hotmail.com

subcontinental lithospheric mantle, in particular during the initial stages, remain poorly constrained. For instance, strength envelopes calculated using empirical flow laws for olivine deformation (e.g. Brace & Kohlstedt, 1980) as well as stresses obtained in numerical models using constant velocity boundary conditions (e.g. England, 1983) indicate that the strength of a 100 km thick continental plate is superior to the stresses that may be produced by mantle convection (<500 MPa; Rolf & Tackley, 2011).

The deformation regimes allowing for thinning of the subcontinental mantle are another poorly constrained issue. Conceptual models propose either pure (McKenzie, 1978) or simple shear (Wernicke, 1981, 1985). Lithospheric-scale thermomechanical models of continental extension (e.g. Lavier & Manatschal, 2006; Huismans & Beaumont, 2007) often show development of asymmetric normal shear zones into the lithospheric mantle, consistent with simple shear conceptual models. Extensional shear zones with thicknesses ranging from hundreds of metres to a few kilometres wide have been mapped in peridotite massifs (Dijkstra *et al.*, 2004; Kaczmarek & Tommasi, 2011; Vauchez *et al.*, 2012; and references therein). However, analysis of shear wave splitting data in continental rifts suggests that the lithospheric mantle in continental rifts deforms not by pure or simple shear, but by transtension (Vauchez *et al.*, 2000). Numerical models that consider explicitly the effect of olivine crystal preferred orientations on the mechanical behavior of the lithospheric mantle show that transtension is favoured when pre-existing lithospheric-scale strike-slip faults or transpressional belts are reactivated in response to extensional boundary conditions (Tommasi *et al.*, 2001, 2009).

Although the tectonic processes that resulted in their emplacement into the crust might result in solid-body rotations, which prevent direct interpretation of the kinematics of the mantle deformation, peridotite massifs allow integration of observations of the deformation of the subcontinental mantle lithosphere from the micrometre to the kilometre scale. Their study provides constraints on both the deformation processes and regimes active in the lithospheric mantle. Among the various peridotite massifs that crop out in orogenic belts worldwide, the Ronda and Beni Bousera 'twin' orogenic peridotites in the Betic–Rif belt of southern Spain and northern Morocco provide a unique opportunity to study the thinning and exhumation of initially thick subcontinental mantle, as they preserve kilometre-scale petrological zoning, which records the polybaric and polythermal evolution of the peridotites and associated pyroxenites (e.g. Obata, 1980; Kornprobst *et al.*, 1990; Targuisti, 1994; van der Wal & Vissers, 1996; Lenoir *et al.*, 2001; Frets *et al.*, 2012). However, a simple tectonic model explaining this tectono-thermal evolution is still lacking.

Here, we present a petrological–structural study of the Beni Bousera orogenic peridotite massif, which includes (1) field mapping of the ductile deformation structures and metamorphic assemblages at the scale of the massif, (2) analysis of the microstructures and crystal preferred orientations in more than 100 peridotite samples, and (3) determination of equilibration temperatures across the massif. This joint analysis of the deformation and metamorphic evolution allows us to propose that the entire Beni Bousera massif constitutes an exhumed low-angle shear zone responsible for thinning and fast exhumation of deep levels of the subcontinental lithospheric mantle, probably accompanied by extensive belt-parallel flow.

GEOLOGICAL SETTING

The Beni Bousera massif crops out at the base of the internal zones of the Alpine Rif belt of northern Morocco (Fig. 1a; Kornprobst, 1974; Michard *et al.*, 1997). Two metamorphic ensembles form these internal zones (Fig. 1b). The upper unit, the Ghomarides, is composed of Palaeozoic to Tertiary sediments metamorphosed under low-pressure, low-temperature conditions during the Variscan orogeny (Chalouan & Michard, 1990) and partly overprinted by an Alpine metamorphic event (Negro *et al.*, 2006). The lower unit, the Sebtides, is characterized by a strong metamorphic gradient; peak temperature conditions change over less than 5 km from 500–550°C at 0·7–0·8 GPa in the topmost Filali schists to up to 800–850°C at 1·0–1·3 GPa in the garnet granulites that crop out at the contact with the Beni Bousera peridotites (Chalouan *et al.*, 2008; and references therein). Foliations and lineations are, however, consistent over the entire unit. Foliations dip shallowly towards the SW on average (Fig. 1b; Kornprobst, 1974; Saddiqi, 1995; Negro *et al.*, 2006; Afiri *et al.*, 2011). Lineations trend NW–SE on average, with a dominant top-to-the-NW sense of shear (Saddiqi *et al.*, 1988; Negro *et al.*, 2006; Afiri *et al.*, 2011). The age and significance of lower Sebtides metamorphism are controversial (Chalouan *et al.*, 2008; and references therein), but it probably records an evolution in which a Variscan HP–HT metamorphism (Bouybaouène *et al.*, 1998; Montel *et al.*, 2001; Rossetti *et al.*, 2010) was overprinted by a late high-temperature Alpine event related to the exhumation of the mantle peridotites (Janots *et al*, 2006; Negro *et al.*, 2006; Afiri *et al.*, 2011).

Previous studies on the Beni Bousera peridotite focused mainly on the geochemistry and petrology of pyroxenites (Kornprobst, 1969, 1970; Pearson *et al.*, 1989, 1991, 1993; Kornprobst *et al.*, 1990; Gueddari *et al.*, 1996; Kumar *et al.*, 1996; Pearson & Nowell, 2004; El Atrassi *et al.*, 2011; Gysi *et al.*, 2011) and, to a lesser extent, peridotites (Kornprobst, 1969; Targuisti, 1994). Fewer studies analysed the structure of the peridotites and pyroxenites (Kornprobst, 1969; Reuber *et al.*, 1982; Saddiqi *et al.*, 1988; Frets *et al.*, 2012). Kornprobst (1969) proposed that the Beni Bousera massif recorded a polybaric evolution starting at depths >150 km.

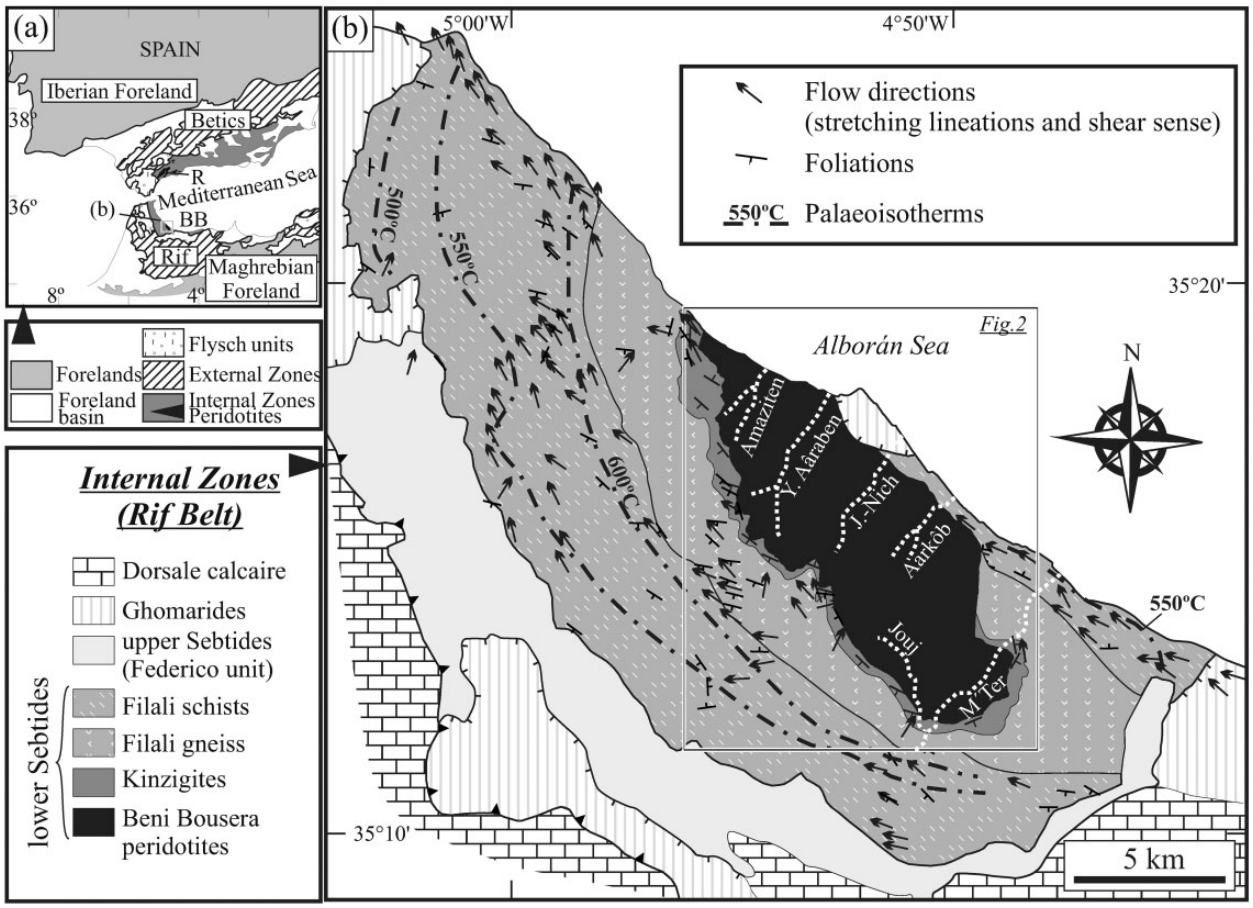

Fig. 1. (a) Simplified map of the Rif–Betic mountain belt showing the location of the Beni Bousera (BB) and Ronda (R) peridotite bodies. (b) Simplified geological map of the Internal Zones of the Rif belt. Flow directions and foliations in the lower Sebtides crustal units are from Kornprobst (1969), Saddiqi *et al.* (1988), Negro (2005), Negro *et al.* (2006) and Afiri *et al* (2011). Palaeo-isotherms in the Sebtides are peak Raman spectroscopy on carbonaceous material (RSCM) temperatures from Negro *et al.* (2006).

Reuber *et al.* (1982) produced the first detailed structural map of the massif and proposed that the peridotites recorded pre-Alpine lithospheric thinning followed by thrusting in the Mesozoic. Saddiqi *et al.* presented a similar interpretation. More recently, comparison of the structures in the peridotites and overlying crustal units led Afiri *et al.* (2011) to propose that the peridotites were exhumed in the footwall of a lithospheric extensional shear zone.

METHODS

Structural mapping

We conducted petrological–structural mapping of the massif and microstructural analysis of more than 100 oriented peridotite samples collected mainly along valleys roughly perpendicular to the long axis (and to the structural grain) of the massif that provide almost continuous outcrops of fresh peridotite (Fig. 2). Field measurements of the foliation and lineation were complemented by measurements of the shape preferred orientation (SPO) of olivine grains derived from automatic grain boundary mapping of oriented thin sections. We also used the crystallographic preferred orientations (CPO) of olivine and pyroxenes to check the orientations of the foliation and lineation. Because olivine and pyroxenes exhibit few slip systems with highly variable strengths, the dominant slip direction tends to align parallel to the shear direction (or stretching lineation) and the slip plane to the shear plane or foliation during simple or pure shear deformation (Zhang & Karato, 1995; Tommasi *et al.*, 2000; Bystricky *et al.*, 2000). Therefore, where a lineation associated with an elongation of pyroxenes or with an alignment of spinels could not be observed in the field, lineation directions were inferred from the maximum concentration of olivine [100] and of pyroxenes [001] axes.

Mineral chemistry

Major element mineral compositions (Supplementary Data Appendix 1; all supplementary material is available for downloading at http://www.petrology.oxfordjournals.

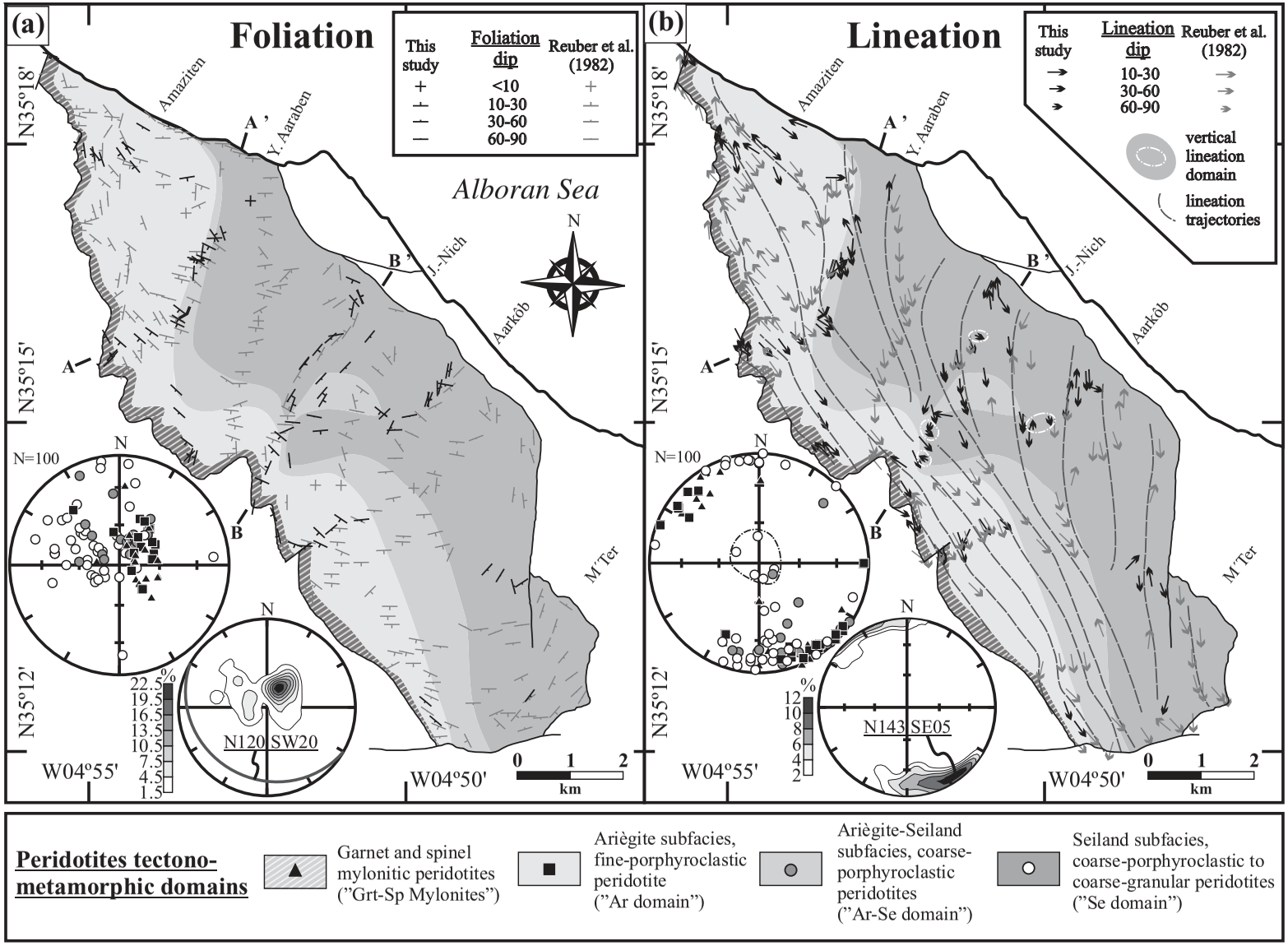

Fig. 2. Structure of the Beni Bousera peridotite. (a) Map of foliations based on original data collected in this study and by Reuber *et al.* (1982). The tectono-metamorphic domains are represented in the background. Lower hemisphere stereoplots on the lower left show the poles of foliation measured in this study as a function of the tectono-metamorphic domain and their density contours. (b) Map of lineations and lineation trajectories based on original data collected in this study and by Reuber *et al.* (1982). The dip direction of lineations from Reuber *et al.* (1982) was inferred from the dip of neighbouring foliations. Lower hemisphere stereoplots show the lineations measured in this study as a function of the tectono-metamorphic domain and their density contours. The progressive clockwise rotation of the lineation orientation from shallowly dipping towards the SE in the mylonites and Ar domain to more south to SSE directions in the Se domain should be noted. Subvertical lineations in the Se domain are highlighted in the map and the stereoplot by dashed lines. All foliation and lineation data from this study were checked by comparison between field measurements and CPO data on oriented thin sections.

org) were acquired by electron microprobe analysis (EPMA) using a CAMECA SX100 at the 'Microsonde Sud' facility, University of Montpellier 2 (Montpellier, France) and the CIC of the University of Granada (Granada, Spain). Analytical conditions used were an accelerating voltage of 20 kV, a 10 nA focused beam, and counting times of 20–30 s.

Crystallographic preferred orientations (CPO)

CPO of olivine, orthopyroxene and clinopyroxene were obtained by indexing electron back-scattered diffraction (EBSD) patterns generated using a JEOL JSM 5600 or a CamScan Crystal Probe X500 scanning electron microscope at Geosciences Montpellier (Université de Montpellier 2, Montpellier, France). An acceleration voltage of 17 kV and a working distance of 23 mm were used. The CHANNEL+ software (Oxford-HKL Technology) was used for CPO indexing and acquisition. Orientation maps covering 25–90% of the thin section were obtained in automatic acquisition mode with a step size of 12–100 μm, depending on grain size (step size was always at least five times smaller than the average recrystallized grain size). Standard post-acquisition data treatment for olivine-rich rocks (see Tommasi *et al.*, 2008) allowed the proportion of indexed points to be increased. All CPO are shown in the geographic reference frame on equal area lower hemisphere stereonets. They are plotted as one average orientation measurement per grain to avoid oversampling of larger crystals and are density contoured when more than 100 grains could be measured in the thin section.

The CPO strength was determined using the J-index, which is the volume-averaged integral of the squared orientation densities (Bunge, 1982). The J-index ranges between unity for a random distribution and infinity for a single crystal, but in practice it has a maximum of around 250 owing to truncation at expansion 22 of the spherical harmonic series (Ben Ismail & Mainprice, 1998). The J-index was calculated for the one orientation per pixel data using the SuperJ software by D. Mainprice (ftp://www.gm.univ-montp2.fr/mainprice//CareWare_Unicef_Programs/) with a 10° Gaussian half-width, data at 1° bins, and truncation of the orientation distribution function at degree 22. We calculated the J-index using one orientation per pixel instead of one orientation per grain, because this allows the CPO strength to be related to the microstructure (large porphyroclasts contribute more to the J-index, as they do for the anisotropy of physical properties). Moreover, grain detection in altered samples might be biased, as crystals containing fractures filled by alteration products are not identified as a single grain.

To characterize the symmetry of the olivine CPO the BA-index was used. This index is based on the LS-index proposed by Ulrich & Mainprice (2005). It is calculated as

$$\text{BA-index} = \frac{1}{2}\left\{2 - \left[\frac{P_{010}}{(G_{010} - P_{010})}\right] - \left[\frac{G_{100}}{(G_{100} - P_{100})}\right]\right\} \quad (1)$$

where P and G are the point and girdle fabric indices (Vollmer, 1990) for the crystallographic axes [100] and [010]. These indices are calculated using the MTEX software (Hielscher & Schaeben, 2008; Bachmann *et al.*, 2010). For each axis, the orientation tensor and its three eigenvalues λ_1, λ_2, λ_3 (where $\lambda_1 \geq \lambda_2 \geq \lambda_3$ and $\lambda_1 + \lambda_2 + \lambda_3 = 1$) are used to determine

$$P = \lambda_1 - \lambda_2 \text{ and } G = 2(\lambda_2 - \lambda_3). \quad (2)$$

For a perfect axial-[010] CPO, the P and G values for [010] and [100] are 1, 0 and 0, 1 respectively, and the BA-index is 0. In the other end-member case, a perfect axial-[100] CPO, the P and G values for [100] and [010] are 1, 0 and 0, 1, respectively, and the BA-index is 1.

Olivine grain-size distributions and aspect ratios

We computed the area-weighted grain size (equivalent circular diameter), grain-size distributions and aspect ratios of olivine from digital EBSD grain boundary maps of 29 samples distributed along three valleys (Aâraben, Aarkôb, and J. Nich) crosscutting the massif (Fig. 2) using the MTEX software (Hielscher & Schaeben, 2008; Bachmann *et al.*, 2010). Area-weighted grain-size distributions are skewed to smaller grain-size classes relative to volume-weighted grain-size distributions (e.g. Higgins, 1994; Garrido *et al.*, 2001); they are therefore solely used to describe comparatively the variation of the microstructure across the massif. For this analysis, non-indexed areas in the EBSD maps were automatically filled by extrapolating data from successively 8, 7, 6, 5 neighbouring pixels with identical orientations or, in a few instances, manually. In both cases, extrapolation was controlled by comparison with optical microstructural images.

THE STRUCTURE OF THE BENI BOUSERA PERIDOTITE MASSIF

The Beni Bousera peridotite massif is elongated in the NW–SE direction, parallel to the trend of the orogenic belt (Fig. 1b). To the NE, it is bounded by the present-day coast or by normal faults that place the peridotite in direct contact with sedimentary units of the Ghomarides (Fig. 1b). In all other directions, the peridotite is overlain by garnet granulites ('kinzigites') with foliations subparallel to the contact (Fig. 1b). The peridotite–granulite contacts are often reactivated by small brittle faults accompanied by strong serpentinization.

The orientation of the foliation and lineation is rather homogeneous at the scale of the massif (Fig. 2). Foliations dominantly dip gently (<30°) towards the SW (maximum density at N120E°–20°SW) and contain shallowly dipping SE-trending lineations (maximum density at 5° towards N143°). Local changes of the foliation and lineation orientation near the contact with the crustal units (Fig. 2) may be accounted for by rotations owing to the brittle faults that reactivated these contacts. Most often, the peridotite and granulite foliations at the contacts are subparallel, but not exactly concordant (Fig. 3).

The variability of the foliation direction and dip, which may attain 80° (see the stereogram in Fig. 2a), in the central and northeastern, structurally lower parts of the massif is, however, best explained by metre- to decametre-scale open folds with NNW–SSE-trending axial planes and subhorizontal axes that affect both the foliation and the compositional layering (Fig. 3). These structurally lower parts of the massif are also characterized by a larger variability in the orientation of the lineation, which tends to display SSE to south directions (see the stereogram in Fig. 2b). The changes in the orientation of the lineation across the massif are gradual and continuous (Fig. 2). The exceptions are five small areas (<200 m in diameter) in the centre of the massif, which display subvertical lineations (Figs 2 and 3). The transition between these subvertical lineations to the dominant shallowly dipping ones could not be mapped owing to lack of exposures, but it is rather abrupt, occurring within <50 m.

Despite the homogeneity and continuity of the ductile deformation structures, we mapped, in agreement with Targuisti (1994) and Frets *et al.* (2012), four tectono-metamorphic domains in the Beni Bousera massif based on the mineral assemblages (presence of garnet or spinel in the peridotites or in the associated pyroxenites; see O'Hara, 1967; Obata, 1980) and microstructures (grain-size decrease). The transitions between domains are gradual, and their limits are not emphasized by any structural

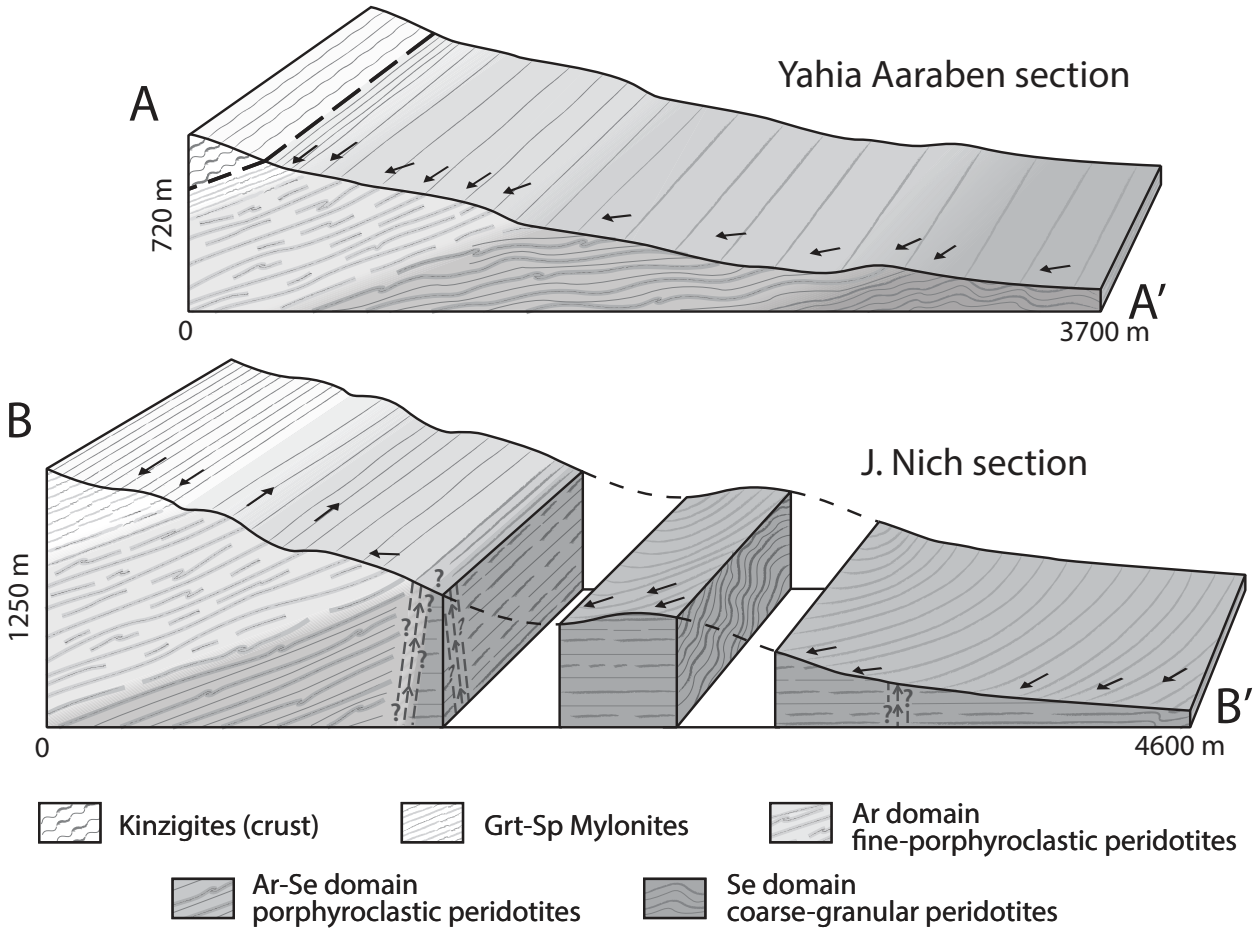

Fig. 3. Geological cross-sections along the Yahia Aâraben (AA') and J. Nich (BB') valleys illustrating the structure of the Beni Bousera massif. The 'Yahia Aâraben' section shows a consistent attitude of the foliation across all domains and illustrates the effect of the open folds on the foliation orientation in the Ar–Se and Se domains. The J. Nich section, which displays a more complex structure, crosscuts three of the four vertical lineation areas mapped in the massif.

discontinuity. From SW to NE and from top to bottom (Fig. 2), the Beni Bousera tectono-metamorphic domains are as follows.

(1) The garnet and spinel mylonites (hereafter referred to as 'Grt–Sp mylonites') that crop out in a 100–200 m wide domain below the contact with the overlying crustal garnet granulites (Figs 2 and 3). This domain is composed of mylonitic garnet–spinel peridotites with a penetrative foliation (Fig. 4a) and a lineation marked by elongated (aspect ratios up to 10:1) orthopyroxene porphyroclasts (Fig. 4b). These peridotites enclose highly stretched and boudinaged garnet pyroxenite layers (1–10 cm wide; Fig. 4b). This deformation locally results in a centimetre-scale layering of garnet-bearing pyroxene-rich and spinel-bearing olivine-rich domains that parallels the peridotite foliation (Fig. 4a). Rare asymmetric orthopyroxene porphyroclasts and pressure shadows around garnets indicate preponderantly a top-to-the-SE shear sense (Fig. 4c).

(2) The Ariègite subfacies domain (hereafter referred to as 'Ar domain') is composed of fine-grained porphyroclastic spinel peridotites with a penetrative foliation and lineation (Fig. 5a and b). These peridotites enclose concordant garnet pyroxenite layers a few centimetres to several decimetres thick, which display sharp contacts with the peridotite (Fig. 5c). The pyroxenites are often boudinaged (Fig. 5c) or isoclinally folded.

(3) The Ariègite to Seiland transition (hereafter referred to as 'Ar–Se domain') is a domain of variable thickness, which ranges from >500 m in the Y. Aâraben valley to <300 m in the J. Nich section (Figs 2 and 3). It is characterized by medium- to coarse-grained porphyroclastic spinel peridotites (Fig. 6a), which enclose centimetre- to decametre-scale pyroxenite layers containing garnet (usually transformed to dark, greenish kelyphite) and coarse spinel (Fig. 6a). The pyroxenites are usually less boudinaged than in the mylonites and Ar domains, but are locally isoclinally folded (Fig. 6b).

(4) The Seiland subfacies domain (hereafter referred to as the 'Se domain') constitutes the lowermost exposed level of the massif (Figs 2 and 3). It is characterized by coarse-grained porphyroclastic peridotites with a foliation defined by a weak shape-preferred orientation of pyroxenes (Fig. 7a) or by granular spinel peridotites containing rounded spinels and centimetre-scale orthopyroxenes (Fig. 7b). Most of the Se domain displays a diffuse centimetre- to decametre-scale compositional layering (from harzburgite to spinel websterite) subparallel to the foliation (Fig. 7c and d). It also comprises decametre- to hectometre-sized areas containing dunite, either concordant with the foliation or forming irregular pods, and greenish spinel websterite layers or lenses with diffuse boundaries with the host peridotite. These websterite layers

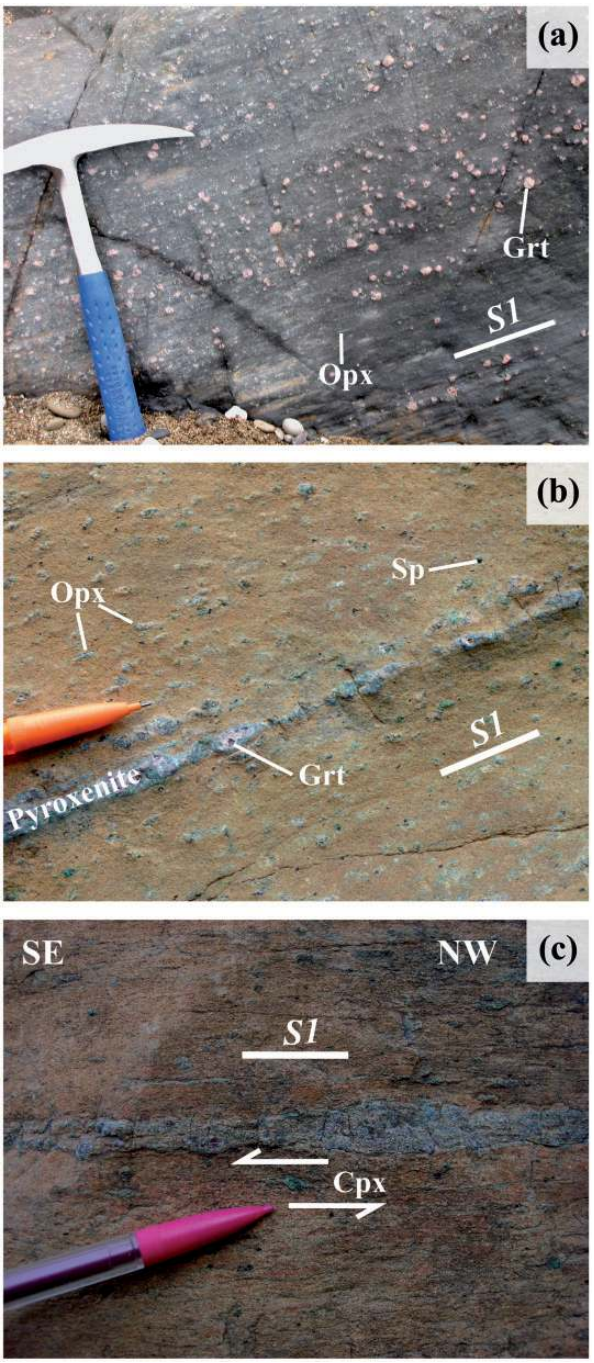

Fig. 4. Macroscopic structures in the Grt–Sp mylonites domain. (a) Grt–Sp peridotite mylonite from the vicinity of the contact with the crustal granulites showing a well-developed foliation (S_1) and lineation marked by elongation of orthopyroxene (Opx) and a diffuse compositional layering parallel to the foliation marked by variations in the content of rounded garnet (Grt) porphyroclasts. (b) Sp peridotite mylonite with elongated orthopyroxenes (Opx) marking the foliation (S_1) and lineation, rounded spinels (Sp), and a thin boudinaged garnet (Grt) pyroxenite layer parallel to the peridotite foliation. (c) Sp peridotite mylonite with a pervasive foliation, enclosing an intrafolially folded and boudinaged Grt-pyroxenite; the asymmetry of pressure shadows on porphyroclasts suggests a top-to-the-SE sense of shear.

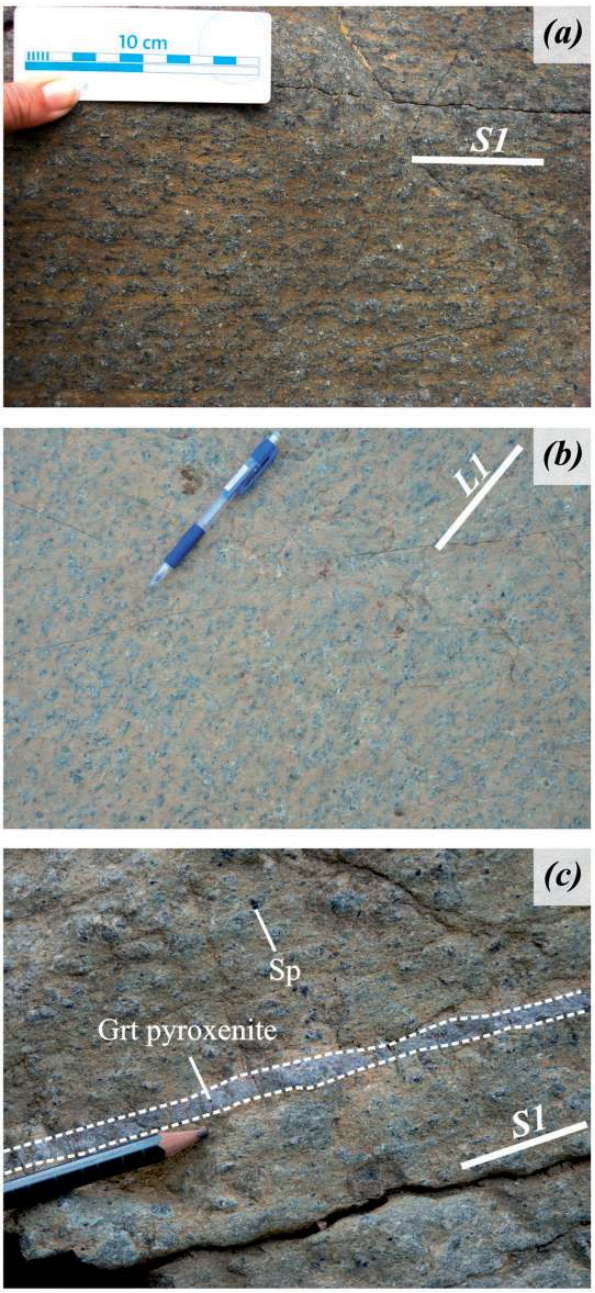

Fig. 5. Macroscopic structures in the Ar domain. (a) Fine-porphyroclastic peridotite displaying a foliation (S_1) and (b) lineation (L_1) marked by the elongation of pyroxenes and spinel in coarse porphyroclastic sp-peridotites from the lower part of the Ar domain. (c) Porphyroclastic sp-peridotite enclosing a centimetre-scale weakly boudinaged Grt-pyroxenite layer parallel to the peridotite foliation (S_1), which is marked by elongation of orthopyroxene. The large rounded spinels (Sp), which may represent pseudomorphs from garnet, in the peridotite should be noted.

are either concordant with or slightly oblique to the peridotite foliation (Fig. 7e and f). Dunites and websterites are particularly abundant in the vicinity of the subvertical lineation areas.

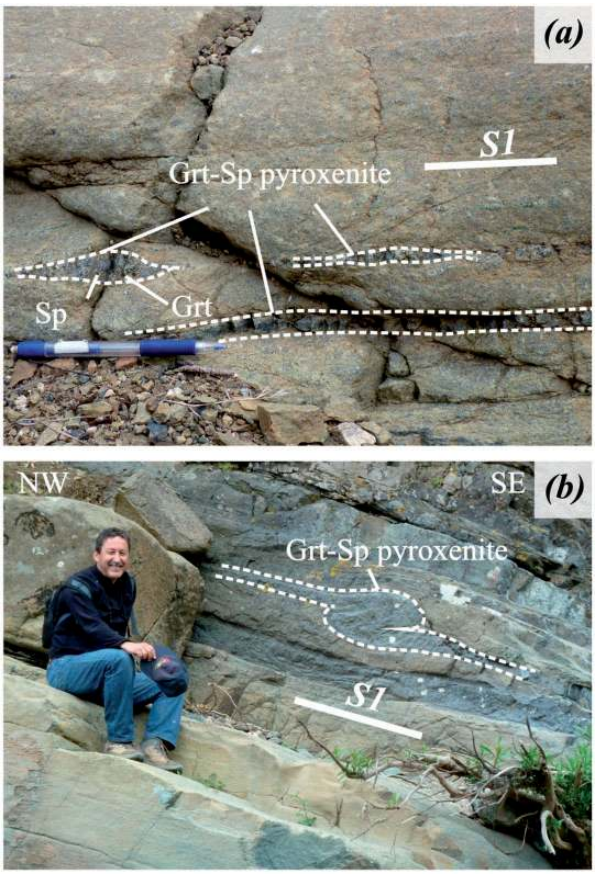

Fig. 6. Macroscopic structures in the Ar–Se domain. (a) Porphyroclastic peridotite enclosing centimetre-scale Grt–Sp pyroxenite lenses parallel to the peridotite foliation (S_1); these lenses were probably formed by extreme boudinage of a formerly continuous pyroxenite layer. (b) Porphyroclastic peridotite with a pervasive foliation enclosing decimetre-scale Grt–Sp pyroxenite layers exhibiting boudinage and asymmetric folds, which indicate a top-to-the-SE shear sense.

MICROSTRUCTURES

The most obvious microstructural variation at the scale of the massif is the increase in the average grain size of olivine from the Grt–Sp mylonites to the Se domain (Fig. 8). The size and relative proportion of olivine porphyroclasts also increases across the massif (Figs 8 and 9). Grt–Sp mylonites and Ar domain peridotites are characterized by a bimodal grain-size distribution in which porphyroclasts are embedded in a finer-grained recrystallized matrix (Fig. 9a–c). Peridotites in the Ar–Se domain are distinguished by the presence of rare, but extremely coarse (centimetre-scale) elongated olivine crystals (Fig. 9d–f). Coarse-granular porphyroclastic peridotites from the Se domain show more homogeneous grain-size distributions (Fig. 9h and i).

Grt–Sp mylonites

Grt–Sp peridotite mylonites are characterized by millimetre-sized garnet and pyroxene porphyroclasts (Figs 9a, b

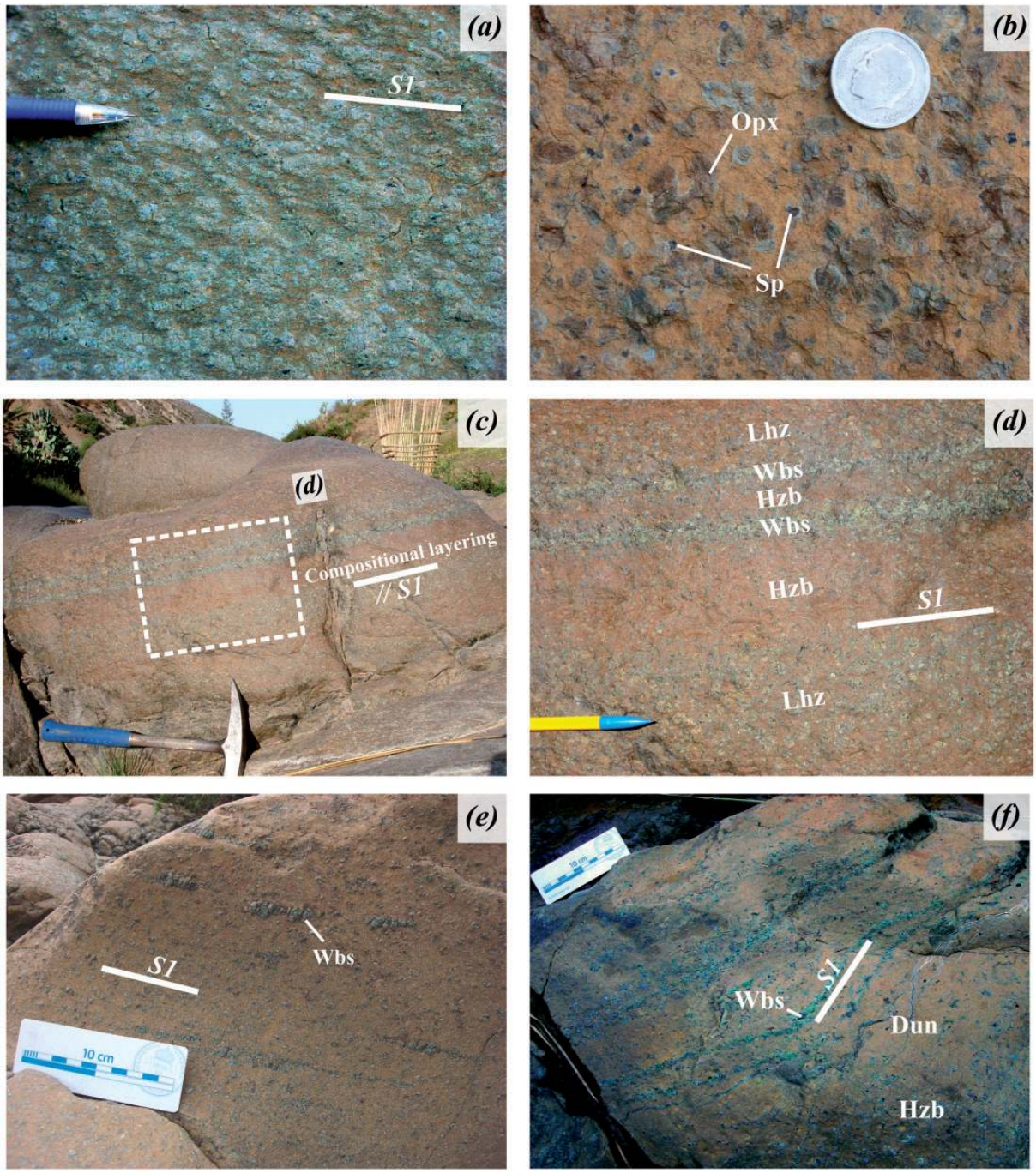

Fig. 7. Macroscopic structures in the Se domain. (a) Coarse-porphyroclastic lherzolite with a foliation (S_l) marked by a weak shape preferred orientation of the pyroxenes. (b) Coarse-granular peridotite from the vicinity of the Ar–Se transition displaying centimetre-size orthopyroxenes (Opx) and coarse rounded spinels (Sp) with greenish pyroxene rims. (c, d) Diffuse compositional layering parallel to the foliation (S_l). Lhz, lherzolite; Wbs, sp-websterite; Hzb, harzburgite. (e) Spinel-websterite (Wbs) lens aligned in the peridotite foliation (S_l) within a dunitic to harzburgitic level near the contact with the Ar–Se domain. (f) Diffuse harzburgite (Hzb)–dunite (Dun)–websterite (Wbs) layering parallel to the peridotite foliation (S_l).

and 10) embedded in a fine-grained matrix of spinel, olivine and pyroxene neoblasts, which show a weak shape-preferred orientation marking the mylonitic foliation (Fig. 10a). Olivine is almost totally recrystallized (average grain sizes of 90–160 μm; Figs 8 and 9a, b). Average aspect ratios range between 1·7 and 2 for all grain-size populations. Olivine crystals have irregular shapes with serrated grain boundaries and undulose extinction

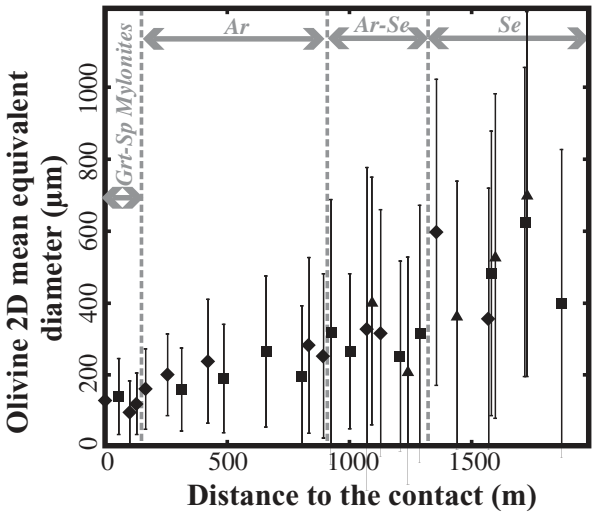

Fig. 8. Olivine area-weighted equivalent grain diameter (grain size) as a function of the distance to the contact with the crustal granulites, measured normal to its average N30W–30°SE orientation. Bars represent the standard deviation. The correlated increase in average grain size and variability with increasing distance from the contact should be noted. Diamonds, Yahia Aâraben section; squares, Nich section; triangles, Aârkôb section.

(Fig. 10a, d and e). High-resolution EBSD grain boundary maps reveal the presence of subgrains in olivine crystals irrespective of their size (highlighted in Fig. 10b). In larger crystals, subgrain boundaries are predominantly oriented at a high angle to the grain elongation.

Garnet is concentrated in millimetre-sized, clinopyroxene-rich lenses parallel to the foliation (Figs 9a, b and 10a). Garnet porphyroclasts are usually rounded (Figs 9a, b and 10) and often partly transformed to kelyphite (Fig. 10b). They have irregular grain boundaries with embayments filled with pyroxenes (Fig. 10a) and show pressure shadows filled by olivine with a coarser grain size (Fig. 10b, upper right corner). Garnet occasionally contains reddish-brown spinel (Fig. 10c), pyroxene, and olivine inclusions. Reddish-brown spinel also occurs in the matrix as holly-leaf-shaped crystals (0·2–2 mm) elongated parallel to the foliation.

Orthopyroxene porphyroclasts are often strongly elongated (aspect ratios up to 10:1, Fig. 10d). They commonly show undulose extinction and kink bands at a high angle to clinopyroxene exsolution (Fig. 10e). Orthopyroxene grain boundaries are irregular with embayments filled by olivine (Fig. 10f). Clinopyroxene porphyroclasts are smaller and less elongated than orthopyroxene, but also show undulose extinction. Both pyroxenes occur intermixed with olivine in the matrix as fine-grained crystals (<1 mm) with irregular shapes and sinuous grain boundaries (Fig. 10b), forming clinopyroxene- or orthopyroxene-rich domains aligned parallel to the foliation (Figs 9a, b and 10b).

Arièǵite domain

Fine-grained porphyroclastic peridotites from the Ar domain have a bimodal texture characterized by millimetre-sized olivine and pyroxene porphyroclasts embedded in a fine-grained recrystallized matrix of olivine and pyroxenes (Fig. 9c). The shape-preferred orientation of both porphyroclasts and matrix crystals and the alignment of holly-leaf-shaped spinels define the foliation and the lineation (Figs 9c and 11a–c).

Olivine porphyroclasts and matrix crystals have serrated grain boundaries, undulose extinction, and closely spaced subgrains at a high angle to their elongation (Figs 9c and 11a–c). The olivine mean grain size increases from ~175 μm to >250 μm as a function of the distance from the Grt–Sp mylonites (Fig. 8). The proportion of porphyroclasts also increases.

Orthopyroxene occurs as elongated porphyroclasts that exhibit undulose extinction, kink bands, and pervasive clinopyroxene exsolution (Figs 9c and 11b). Grain boundaries are very irregular, with small embayments (Fig. 11b) or flame-like indentations filled with olivine (Fig. 11c). Clinopyroxene occurs either as isolated crystals or as aggregates; it has irregular shapes and sinuous grain boundaries (Fig. 9c). Spinel is coarser (0·5–2 mm) and has darker colours than in the Grt–Sp mylonites. It occurs as holly-leaf-shaped crystals.

Arièǵite to Seiland transition

Ar–Se domain peridotites show porphyroclastic textures characterized by coarser average olivine grain sizes (250–350 μm; Fig. 8) and lower volume fractions of neoblasts than Ar domain peridotites. A characteristic feature of these peridotites is the presence of large (up to 1 cm), irregularly shaped, elongated crystals of olivine (aspect ratio up to 4:1, Fig. 9d–f) with sinuous grain boundaries within a heterogeneous, coarse-grained olivine-rich matrix (Fig. 9d–f). These crystals appear as isolated spikes in the larger size classes in the area-weighted olivine grain-size distribution (Fig. 9d–f). Both olivine porphyroclasts and neoblasts display undulose extinction and well-developed subgrain boundaries normal to the grain elongation (Figs 9d–f and 11d). Olivine–olivine grain boundaries are usually lobate, but triple junctions and straight grain boundaries are observed locally (Fig. 11d).

Orthopyroxene porphyroclasts are coarser (up to 4 mm) and less elongated than in the overlying domains (Figs 9d–f and 11e). They have very irregular shapes with grain boundary embayments filled by olivine (Fig. 11e). Clinopyroxene has smaller grain sizes, similar to those in Ar domain fine-grained porphyroclastic peridotites. Clinopyroxene occurs mainly as aggregates elongated parallel to the foliation (Fig. 9e and f) or in lens-shaped websteritic aggregates (Fig. 11f). Both pyroxenes have undulose extinction, but kink bands in orthopyroxene are less

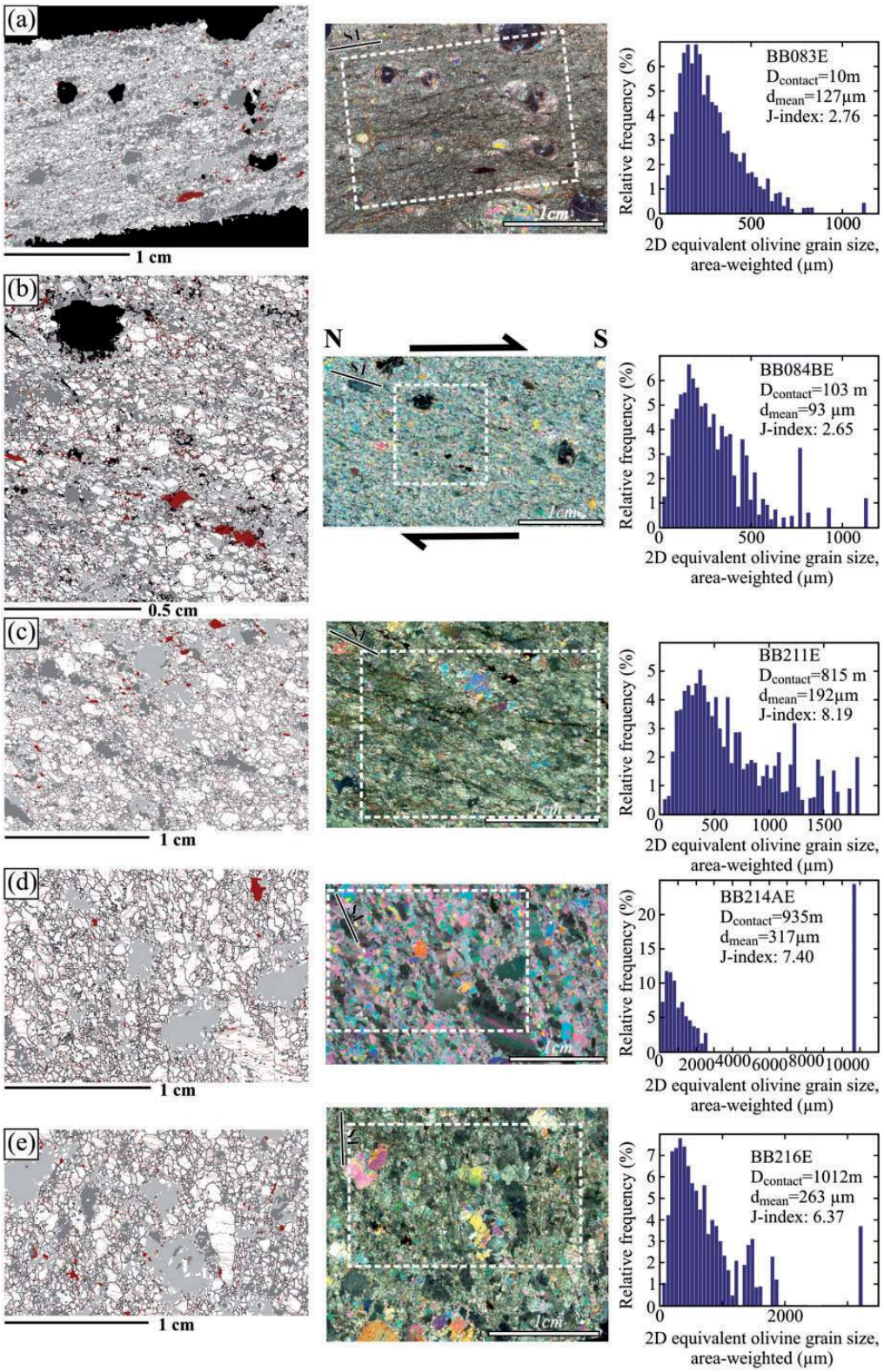

Fig. 9. Microstructural evolution from the Grt–Sp mylonites to the Se domain. Left column: EBSD map showing the phases (white, olivine; light grey, orthopyroxene; dark grey, clinopyroxene; maroon, spinel; black, non-indexed), grain boundaries (misorientations >15° in black), and subgrain boundaries (misorientations >3° in dark red). Centre column: cross-polarized light photomicrographs. Dashed square marks the area mapped by EBSD. S_I indicates the trace of the foliation on the thin section. Right column: area-weighted grain-size distribution of olivine. (a, b) Grt–Sp mylonites. (c) Fine-grained porphyroclastic peridotite from the Ar domain. (d–g) Porphyroclastic peridotites from the Ar–Se domain. (h–j) Coarse-porphyroclastic to coarse-granular peridotites from the Se domain. (See text for further explanation.)

(continued)

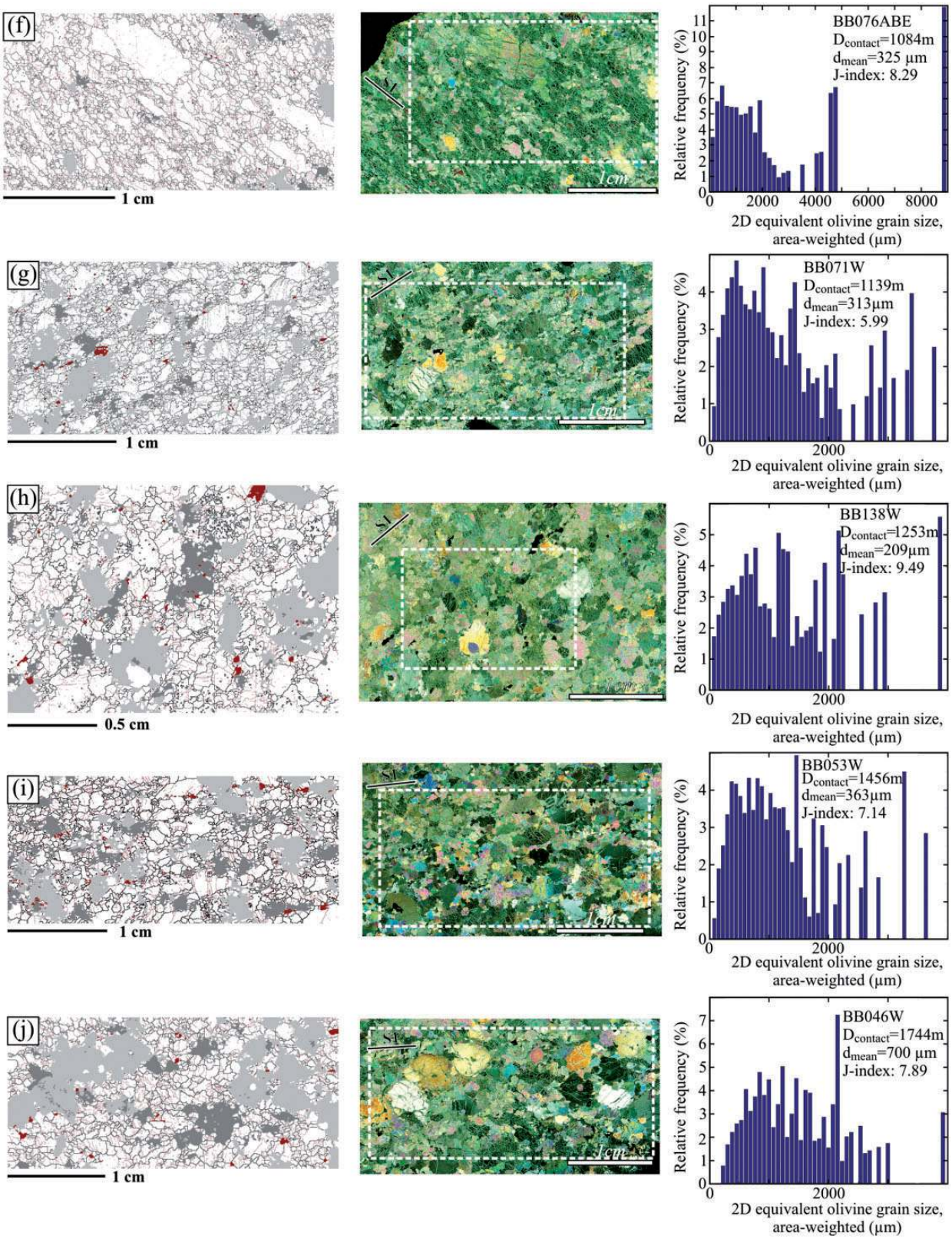

Fig. 9. Continued.

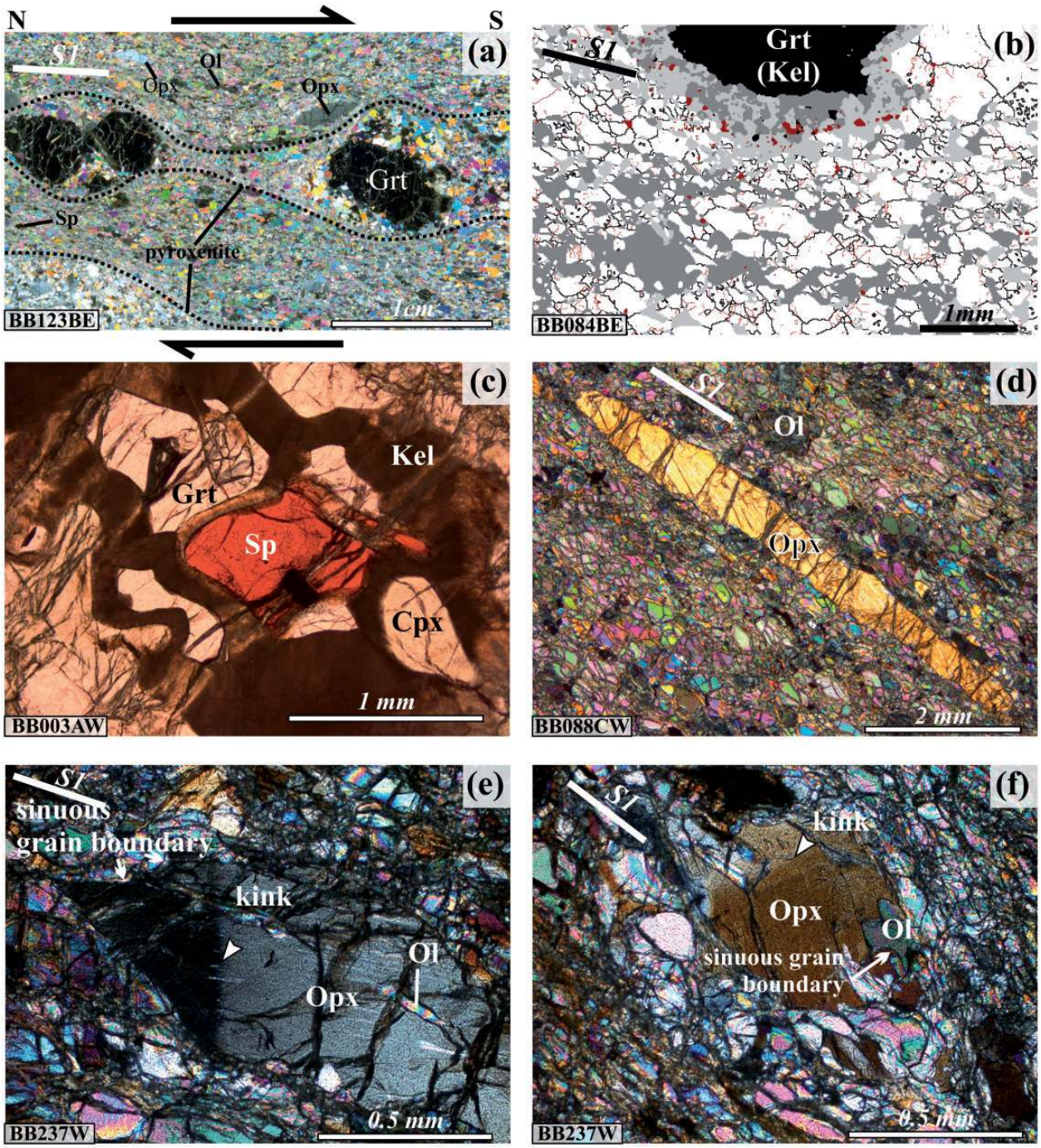

Fig. 10. Microstructures of the Grt–Sp mylonites (a, d–f, cross-polarized light; b, EBSD-based phase and grain boundary map; c, plane-polarized light photomicrograph). (a) Mylonitic peridotite enclosing a strongly boudinaged centimere-scale garnet (Grt) pyroxenite layer; the peridotite foliation, which is marked by the elongation of orthopyroxene (Opx) and olivine (Ol) crystals, wraps around the pyroxenite. The coarser grain sizes in the pressure shadows around garnet crystals should be noted. (b) Detail of phase map from Fig. 9b showing the elongation and subgrains (red lines) in olivine crystals (in white), the irregular shape of pyroxenes (light gray, orthopyroxene; dark gray, clinopyroxene), the compositional layering owing to variation in pyroxene content, and the pyroxene–spinel symplectites (Kel, kelyphite) around garnet. (c) Reddish-brownish spinel (Sp) surrounded by garnet (Grt), clinopyroxene (Cpx) and kelyphite (Kel). (d) Stretched orthopyroxene porphyroclast with a 10:1 aspect ratio marking the lineation. The foliation is marked by the elongation of recrystallized olivine crystals. (e, f) Orthopyroxene porphyroclasts (Opx) showing irregular grain boundaries with embayments and fracture-like features filled by olivine (Ol). In (e) white arrowhead marks kink bands preferentially oriented normal to the clinopyroxene exsolution. The foliation (S_1) is marked by the elongation of olivine crystals.

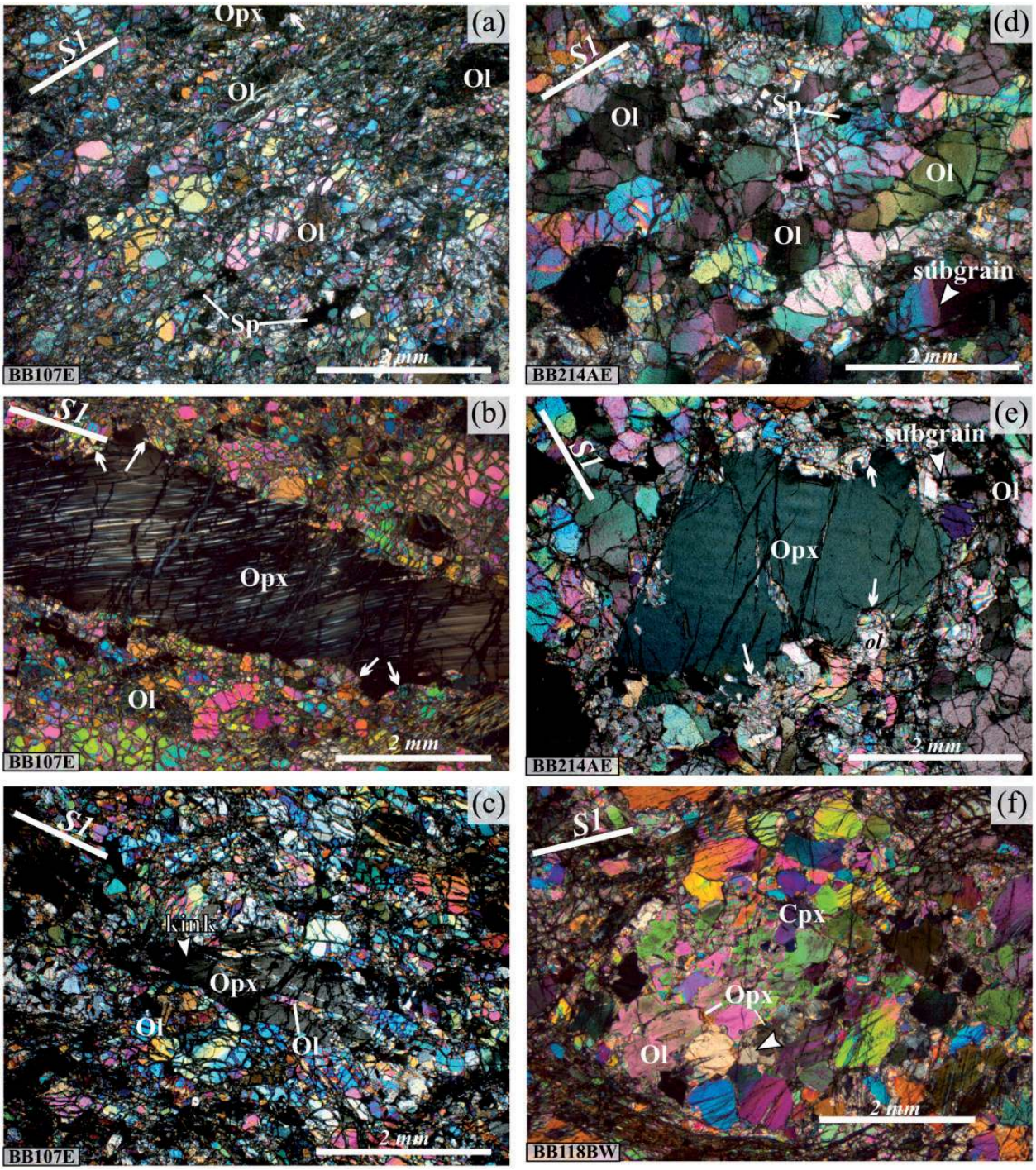

Fig. 11. Microstructures in the Ar (a–c) and Ar–Se (d–f) domain peridotites (cross-polarized light photomicrographs). (a) Fine-grained porphyroclastic peridotite with a foliation (S_1) marked by elongated olivine (Ol) and spinel (Sp) crystals. (b, c) Large elongated orthopyroxene porphyroclasts (Opx) with thin exsolution lamellae showing the bending of the crystalline network, undulose extinction, and irregular grain boundaries with embayments filled by olivine (Ol). White arrows indicate sinuous grain boundaries. (d) Porphyroclastic peridotite with a foliation marked by the shape-preferred orientation of olivine crystals (Ol) with undulose extinction, subgrains aligned normal to the elongation of the crystals and serrated grain boundaries. Spinels (Sp) have rounded shapes. (e) Orthopyroxene porphyroclast (Opx) with irregular grain boundaries filled by olivine (Ol), marked by the arrows. (f) Millimetre-scale websteritic lens, composed of clinopyroxene (Cpx), orthopyroxene (Opx), olivine (Ol), and spinel with interpenetrating grain boundaries, in a coarse-porphyroclastic peridotite. Kink in orthopyroxene (white arrowhead) should be noted.

frequent than in Grt–Sp mylonites and Ar domain peridotites. Spinel occurs as large holly-leaf-shaped crystals (Fig. 9d–f) or as small rounded grains, often included in olivine (Fig. 11d).

Seiland domain

The transition to the Se domain is characterized by a marked increase in the average olivine grain size (Fig. 8). Se domain peridotites have coarse-grained porphyroclastic (Fig. 9h) to coarse-granular textures (Fig. 9i and j). In the former, the foliation and lineation are defined by a weak shape-preferred orientation of olivine and orthopyroxene and by the alignment of spinels (Fig. 9h). The coarse-granular peridotites have bell-shaped area-weighted grain-size distributions, without a clear dominant grain size; area fractions occupied by small and large grains tend to be similar (Fig. 9i and j). They often do not show any clear foliation or lineation.

Olivine crystals of all sizes show very sinuous grain boundaries, undulose extinction, and ubiquitous subgrains (Figs 9h–j and 12a, b). Orthopyroxene is very coarse (up to 8 mm). It has very irregular shapes, with grain boundary embayments or fracture-like features filled with olivine in optical continuity with larger crystals displaying well-developed subgrains (Fig. 12a–c). Coarse orthopyroxene crystals usually have fine clinopyroxene exsolution lamellae, undulose extinction and kink bands (Fig. 12c). Clinopyroxene (Fig. 12a and d) occurs as irregularly shaped, isolated crystals with exsolution lamellae and undulose extinction. Spinel usually occurs as irregular, holly-leaf-shaped grains (Fig. 12a), but large (>2 mm wide) subhedral spinel crystals surrounded by weakly deformed two-pyroxene coronae were observed locally (Fig. 12d).

GEOTHERMOMETRY

Previous geothermobarometric studies of the Beni Bousera massif have focused on estimating pressure and temperature equilibration conditions of the Grt–Sp mylonites (Tabit *et al.*, 1997; Afiri *et al.*, 2011) and pyroxenites (Kornprobst *et al.*, 1990; Frets *et al.*, 2012) as no reliable geobarometric formulation exists for the spinel peridotites that form most of the Beni Bousera massif. Maximum equilibration pressures in Grt–Sp mylonites are *c.* 2·3 GPa (Tabit *et al.*, 1997; Afiri *et al.*, 2011). Slightly lower pressures and moderate temperatures were obtained from the synkinematic assemblages in garnet pyroxenites from the same domain (2·0 GPa and 950°C; Frets *et al.*, 2012). Thermodynamic pseudosection modelling of pyroxenite compositions also provides a lower-bound pressure estimate of 1·8–1·9 GPa and temperatures of 1050–1150°C for the equilibration in the Ar–Se domain (Frets *et al.*, 2012).

To complete this dataset and constrain the thermal evolution of the massif, we carried out a thermometric study on 53 peridotites, sampling all tectono-metamorphic domains. Ca-in-opx temperatures for the Ar, Ar–Se, and Se domain peridotites were calculated using the equation of Brey & Köhler (1990) at $P = 1{\cdot}8$ GPa. Albeit the effect of pressure on Ca-in-opx thermometer is negligible, for accuracy, Ca-in-opx temperatures in Grt–Sp mylonites were calculated for $P = 2{\cdot}0$ GPa, following the synkinematic equilibrium conditions determined for garnet pyroxenites from this domain (Frets *et al.*, 2012). Ca-in-opx temperatures vary continuously from 850 to 1150°C with increasing distance from the contact, except for six samples located in the vicinity of the limit between the Ar–Se and Se domains that yield higher temperatures, >1200°C (Fig. 13; Supplementary Data Appendix 2). These high temperatures might result from excess Ca owing to analysis of tiny clinopyroxene exsolution blebs, but the consistent location of the six samples at the top of the Se domain suggests that their high Ca-in-opx temperature might be the record of a physical process (e.g. local heating associated with melts accumulation), rather than an analysis artefact.

CRYSTALLOGRAPHIC PREFERRED ORIENTATIONS (CPO)

Olivine

The intensity and the symmetry of the olivine CPO vary at the scale of the massif and within each domain. The three most common patterns of olivine CPO in naturally deformed mantle rocks are represented: orthorhombic, axial-[100], and axial-[010]. Axial-[010] olivine CPO patterns are characterized by strong clustering of [010] perpendicular to the foliation and dispersion of [100] and [001] in the foliation plane. Axial-[100] CPO patterns are characterized by a point maximum of [100] parallel to the lineation and a girdle distribution of [010] and [001] normal to it. Orthorhombic olivine CPO patterns are intermediate between the two above end-members, being characterized by point maxima of [100] and [010] parallel to the lineation and normal to the foliation, respectively. Pure axial-[100] or axial-[010] patterns are not observed, but Beni Bousera peridotites show a continuous gradation between the three end-member patterns described above, with a predominance of the axial-[010] component (Figs 14 and 15). Moreover, although the relative intensity of the [100] and [010] maxima varies, all olivine CPO are characterized by clustering of [010] nearly perpendicular to the foliation and of [100] close to the lineation (Fig. 14). [001] is more dispersed, but tends to align at a high angle to the lineation in the foliation plane. Analysis of the obliquity between the olivine CPO and the foliation in the Grt–Sp mylonites and Ar domain peridotites (Fig. 14) suggests dominant top-to-the-SE shear senses, but opposite shear sense or an absence of obliquity is also observed.

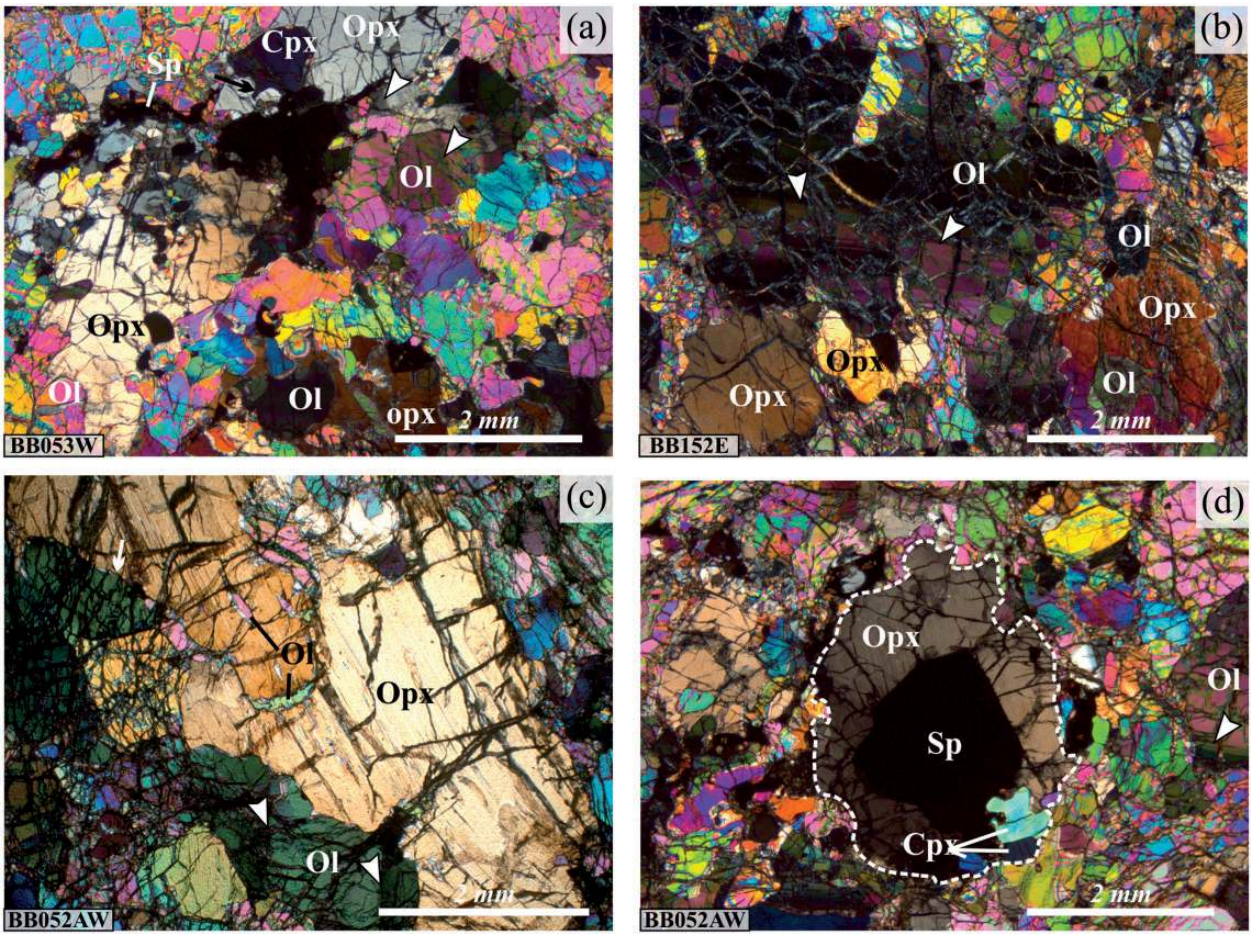

Fig. 12. Microstructures in the Se domain peridotites (cross-polarized light photomicrographs). (a) Olivine (Ol), orthopyroxene (Opx) and clinopyroxene (Cpx) with very irregular shapes and interpenetrating grain boundaries. Olivine crystals show ubiquitous undulose extinction and subgrains. (b) Detail of the same microstructure highlighting a large olivine (Ol) crystal with a very irregular shape, sinuous grain boundaries and closely spaced subgrain boundaries (marked by white arrowheads), as well as irregularly shaped orthopyroxene (Opx) porphyroclasts with embayments filled by olivine. (c) Orthopyroxene porphyroclast (Opx) showing 'fracture-like' features parallel or normal to the exsolution filled by olivine (Ol) 'films' (d) Symplectitic aggregate of spinel (Sp), orthopyroxene (Opx), and clinopyroxene (Cpx). The undulose extinction in the orthopyroxene should be noted.

There is a systematic variation in the olivine CPO pattern at the scale of the massif. Olivine CPO with a strong trend towards axial-[010], indicated by BA-index values <0·4, predominate among the Grt–Sp mylonites (100% of the analysed samples) and the fine-grained porphyroclastic peridotites from the Ar domain (90% of the analysed samples; Fig. 15; Supplementary Data Appendix 3). An exception are two fine-grained porphyroclastic peridotites from the Ar domain that yield olivine CPO patterns with a strong axial-[100] trend (BA-index ~0·7; Fig. 15). With increasing distance from the contact, orthorhombic olivine CPO (0·4 < BA-index > 0·6) and, to a lesser extent, axial-[100] patterns (BA-index >0·6) become more common. Orthorhombic olivine CPO represents roughly half of the measured patterns in the Ar–Se domain and predominates in the Se domain (Fig. 15).

Olivine CPO strength is highly variable; the J-index, which measures the degree of alignment of the CPO, ranges from two, which corresponds to a nearly random distribution, to 15, which indicates a very strong olivine CPO. There is no clear relation between CPO intensity and symmetry, as strong and weak CPO are observed for all symmetries (Fig. 15). Figure 16 shows the evolution of the olivine CPO strength as a function of the distance to the contact for six profiles normal to the massif trend (Supplementary Data Appendix 2). All profiles show similar first-order characteristics. The J-index in Grt–Sp mylonites is usually low, between three and four, except for profile 1 ('Amaziten' valley), where the mylonites have very strong olivine CPO. In the Ar domain, the olivine J-index first increases, reaching values between seven and 14 at ~300 m from the contact, and then decreases more

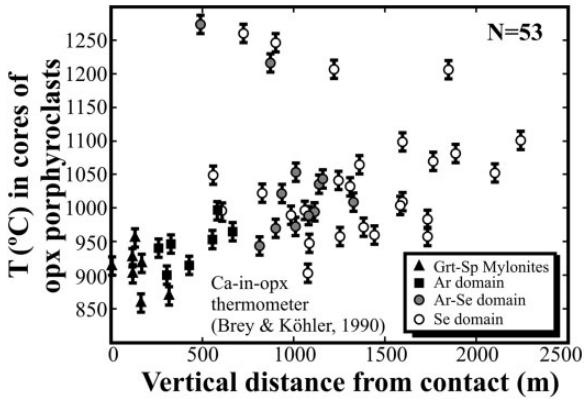

Fig. 13. Equilibration temperatures of the peridotites from the various tectono-metamorphic domains obtained using the Ca-in-opx thermometer (Brey & Köhler, 1990; error ±16°C) on orthopyroxene core compositions as a function of the vertical distance from the contact with the crustal units, measured normal to its average N30W–30°SE orientation.

or less sharply, depending on the profile. The lower part of the Ar domain is usually characterized by rather weak olivine CPO. A second peak in J-index, either sharp or smooth, roughly coincides with the entrance in the Ar–Se domain. Finally, peridotites from the Se domain are characterized by a strong variability in the olivine CPO strength, with J-index values ranging from three to 12.

In Grt–Sp mylonites and Ar domain fine-porphyroclastic peridotites, the intensity of olivine CPO is positively correlated with the average olivine grain size, with the exception of one fine-grained mylonitic peridotite that displays a strong olivine CPO (Fig. 17a). This correlation may account for the increase in J-index from Grt–Sp mylonites to Ar domain peridotites. It cannot, however, explain the decrease in J-index in the lower part of the Ar domain (Fig. 16), as the average olivine grain size increases continuously with increasing distance from the contact (Fig. 8).

The strongest and weakest olivine CPO in Grt–Sp mylonites and Ar domain fine-porphyroclastic peridotites are observed for harzburgites and clinopyroxene-rich lherzolites, respectively, suggesting that the olivine CPO strength is inversely correlated with clinopyroxene modal content (Fig. 17a). Analysis of the entire dataset (Fig. 17b) shows a weak anti-correlation between the clinopyroxene modal content and the olivine CPO strength in the Grt–Sp mylonites to Ar domain peridotites. The relation is, however, not linear and the data show a strong dispersion. In the Ar–Se and Se domains, the olivine CPO strength does not correlate with either the average olivine grain size or the clinopyroxene modal content (Fig. 17a and b).

Pyroxenes

Ortho- and clinopyroxene also display clear CPO, though more dispersed than olivine CPO. Ortho- and clinopyroxene CPO are always correlated (Fig. 14). The pyroxenes CPO is consistent with the olivine CPO in Grt–Sp mylonites and in fine-grained porphyroclastic peridotites from the Ar domain (Fig. 14). In contrast, Ar–Se and Se domain peridotites often show pyroxenes CPO partially or totally uncorrelated to the olivine CPO (Fig. 14). The variations in pyroxene CPO intensity between domains are probably biased by the larger size and lower number of pyroxene crystals in the peridotites from the Ar–Se and Se domains; we focus therefore on the changes in the CPO patterns.

Orthopyroxene and clinopyroxene CPO in the Grt–Sp mylonites and Ar domain show a clustering of [001] subparallel to the lineation and, to a lesser extent, [010] aligned at a high angle to the foliation. Clinopyroxene [100] tends to align at a high angle to the lineation (in particular in the mylonites), whereas orthopyroxene [100] shows no systematic orientation. It may either show a weak concentration normal to the foliation, be dispersed in a girdle normal to the lineation, or display a weak concentration in the foliation plane at a high angle to the lineation.

Pyroxenes in most Ar–Se and Se domain peridotites show two [001] maxima: the usual concentration of pyroxenes [001] sub-parallel to the olivine [100] maximum and, hence to the lineation, and an additional [001] concentration at a low angle to the foliation, but nearly perpendicular to the lineation (compare BB072W and BB059CW in Fig. 14). In some samples, such as BB076CBE, only the [001] maximum at a high angle to the lineation is observed for both ortho- and clinopyroxene. An exception is peridotite BB142A-AW, which has strong ortho- and clinopyroxene CPO well correlated with the olivine CPO. Orthopyroxene [100] and clinopyroxene [010] axes tend to concentrate normal to the foliation, but those samples with a concentration of [001] at a high angle to the lineation also have weak [100] or [010] maxima sub-parallel to the lineation.

DISCUSSION

The Beni Bousera peridotite massif is characterized by a continuous and coupled variation in the metamorphic record and microstructures (equilibration temperatures and grain sizes increase and equilibration pressures decrease) from the Grt–Sp mylonites to the Se domain. Structures are coherent over the entire massif. Except for folded domains, the foliations dip shallowly (<30°) towards the SSW–SW and lineations trend dominantly NW–SE; that is, normal to the metamorphic gradient, with a gradual rotation to a more north–south trend in the lowermost Se domain (Figs 2 and 3). Discontinuities in the metamorphic gradient or crosscutting structures have not been observed. Sharp changes in kinematics are recorded in only four isolated hectometre-scale patches in the Se

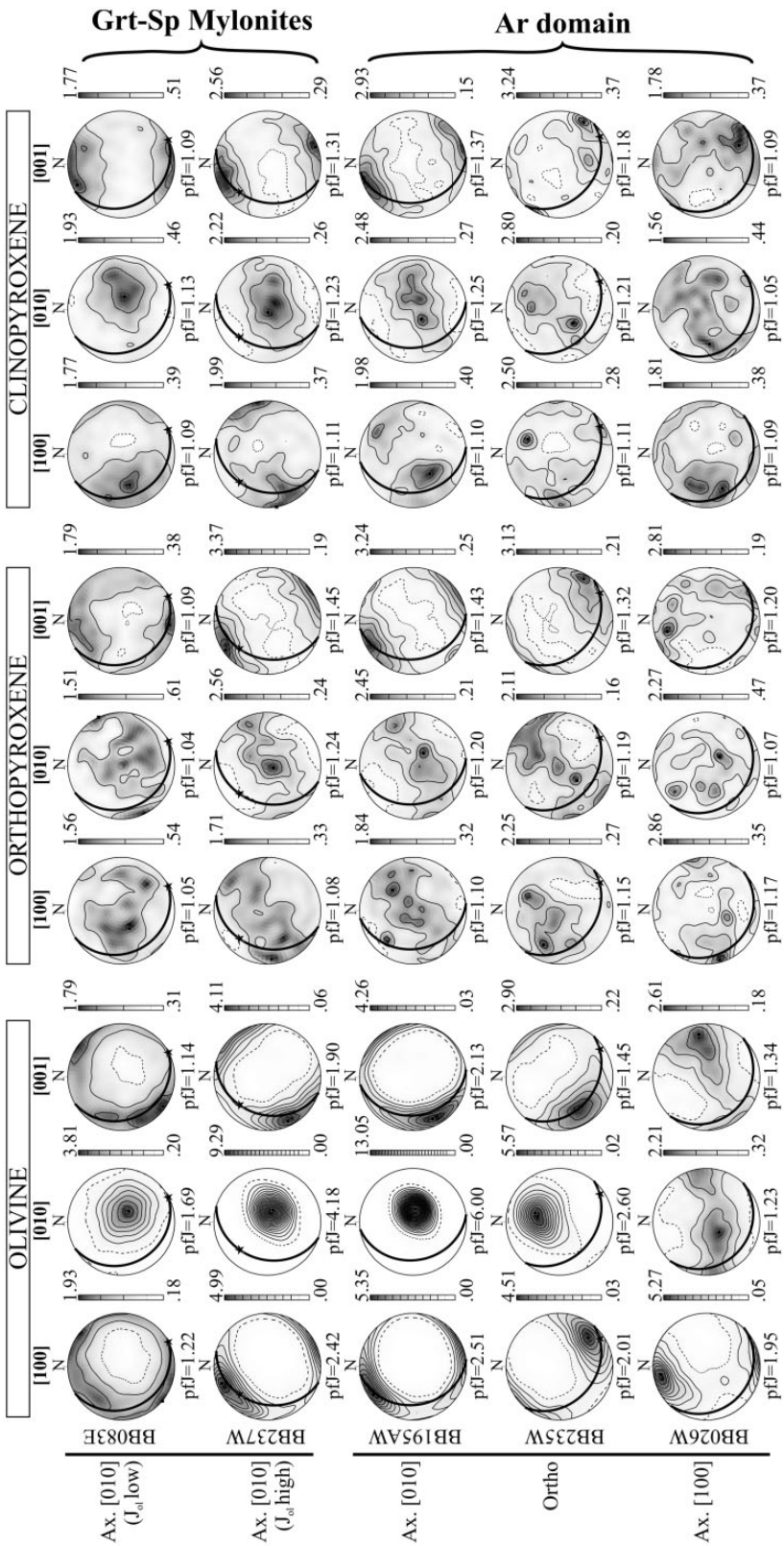

Fig. 14. Olivine, ortho- and clinopyroxene CPO of representative peridotites for all four tectono-metamorphic domains. Lower hemisphere stereoplots; contours at 0·5 multiples of a uniform distribution; inverse log greyscale colouring. Continuous-line and dashed-line black great circles represent the field measurements of the foliation and compositional layering, respectively. Black star marks the field measurement of the lineation.

(continued)

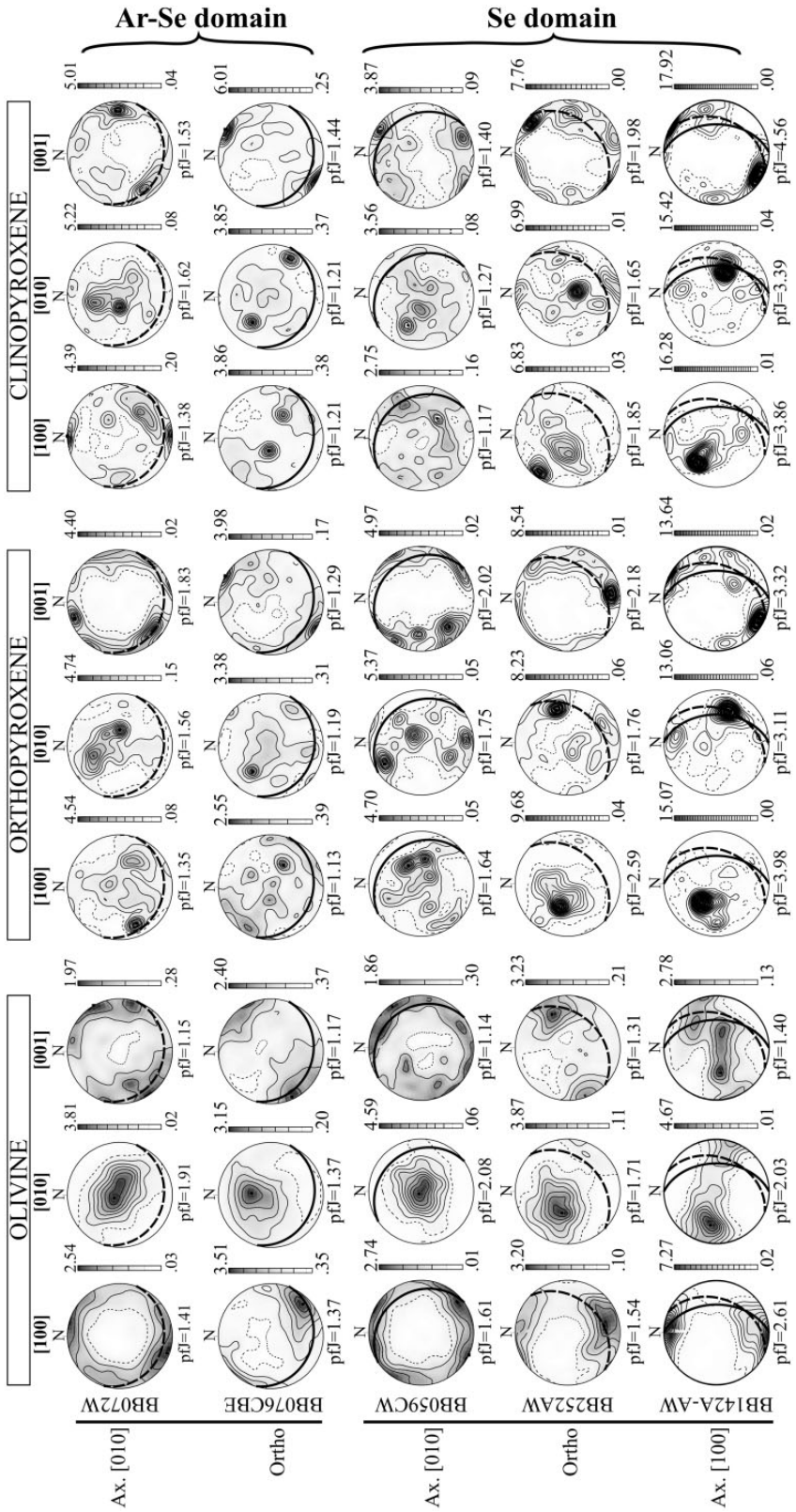

Fig. 14. Continued.

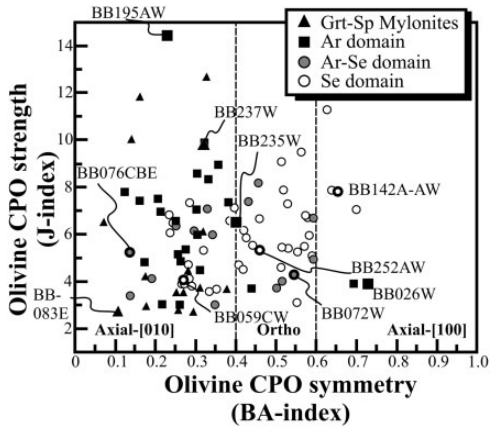

Fig. 15. Olivine CPO strength (quantified by the J-index, which indicates the degree of alignment of the CPO) versus symmetry (characterized by the BA-index) for all Beni Bousera peridotites analysed by EBSD. The continuous evolution from dominant axial-[010] patterns (BA-index <0·4) in the Grt–Sp mylonites and in the Ar domain to dominantly orthorhombic patterns (0·4 < BA-index < 0·6) in the Se domain should be noted. Larger symbols indicate the samples for which the full CPO data are shown in Fig. 14.

domain, which show vertical lineations (Figs 2 and 3). In the following, we first discuss the deformation processes and equilibration conditions in the various tectono-metamorphic domains. This analysis allows us to propose a tectonic scenario explaining the structural and petrological observations. We then discuss the implications of this model for the evolution of the Rif–Betic system.

Deformation mechanisms and conditions

Grt–Sp mylonites: deformation under high stress and low temperature

Peridotites (and pyroxenites; see Frets *et al.*, 2012) from this domain deformed dominantly by dislocation creep, as shown by ubiquitous undulose extinction and subgrains in olivine (Fig. 10b), extreme stretching and kinks in orthopyroxene (Fig. 10c and d), and by the consistent CPO of olivine and pyroxenes (Fig. 14). The fine grain size points to extensive dynamic recrystallization of olivine (Fig. 9a and b). Coexistence of subgrains and recrystallized grains with sizes equivalent to the sinuosity of the olivine grain boundaries (Fig. 10b) suggests that nucleation occurred by subgrain rotation and by bulging.

The well-developed foliation and stretching lineation as well as the intense boudinage of the pyroxenite layers (Fig. 4) imply that Grt–Sp mylonites accommodated large finite strains. Their small grain sizes (mean olivine grain size of 90–160 μm; Figs 8 and 9a, b) imply high plastic work rates (Austin & Evans, 2007), which may be due to high stresses, high strain rates, or both. High stresses are consistent with the low synkinematic temperature conditions recorded in peridotites and garnet pyroxenite layers from this domain (900–950°C; Fig. 13; see also Frets *et al.*, 2012). High stresses (and large finite strains) are also suggested by the intense deformation of the competent (higher strength) garnet pyroxenite layers and by the extreme elongation of orthopyroxene porphyroclasts in the peridotites.

Grt–Sp mylonites show olivine CPO with an axial-[010] symmetry, but with a weak maximum of [100] sub-parallel to the lineation (Fig. 14). Such an olivine CPO may result from three processes: (1) transpressional deformation in which shortening normal to the shear plane is compensated by stretching in multiple directions within the shear plane (Tommasi *et al.*, 1999); (2) simultaneous activation of [100] and [001] glide owing to low temperature–high stress or high pressure (Durham & Goetze, 1977; Mainprice *et al.*, 2005; Demouchy *et al.*, 2013); (3) dynamic or static recrystallization (Tommasi *et al.*, 2008; Falus *et al.*, 2011). The synkinematic pressure of ∼2·0 GPa recorded by the equilibrium mineral assemblages in pyroxenites from this domain (Frets *et al.*, 2012) was too low to produce dominant activation of [001] glide in olivine (>3 or 7 GPa, Jung *et al.*, 2006; Raterron *et al.*, 2009). The remaining processes may all be invoked to account for the axial-[010] symmetry of the olivine CPO in the Grt–Sp mylonites: equilibrium temperatures are low (850–950°C, Fig. 13), stresses were probably high, and olivine is almost totally recrystallized (Fig. 9a and b). The well-developed stretching lineations of the pyroxenes (Fig. 4) and their CPO (Fig. 14), which are consistent with deformation in simple shear with dominant activation of the [001]{110} systems (Bascou *et al.*, 2002), do not point to an oblate strain ellipsoid, but a component of flow normal to the lineation cannot be excluded.

The olivine CPO strength is highly variable (Fig. 15). The positive correlation with the mean olivine grain size (Fig. 18a) points to a recrystallization control on the olivine CPO intensity, higher recrystallized volume fractions leading to more dispersed olivine CPO (Falus *et al.*, 2011). The weak negative correlation between the olivine CPO strength and the clinopyroxene modal content (Fig. 18b) is harder to explain. Similar observations in mantle xenolith suites have been interpreted as the result of dispersion of the olivine CPO associated with reactive melt percolation leading to refertilization (e.g. Tommasi *et al.*, 2008; Morales *et al.*, 2011). In the Grt–Sp mylonites, petrographic features, such as the irregularly shaped pyroxene-rich lenses parallel to the foliation (Fig. 8a and b) and the interpenetrating olivine–pyroxene grain boundaries (Fig. 9b and e), may result from syn- to late kinematic crystallization of pyroxenes at the expense of olivine, probably owing to low-temperature metasomatism by small fractions of fluids or evolved melts, which did not reset the equilibrium temperatures in this domain (850–950°C; Fig. 13).

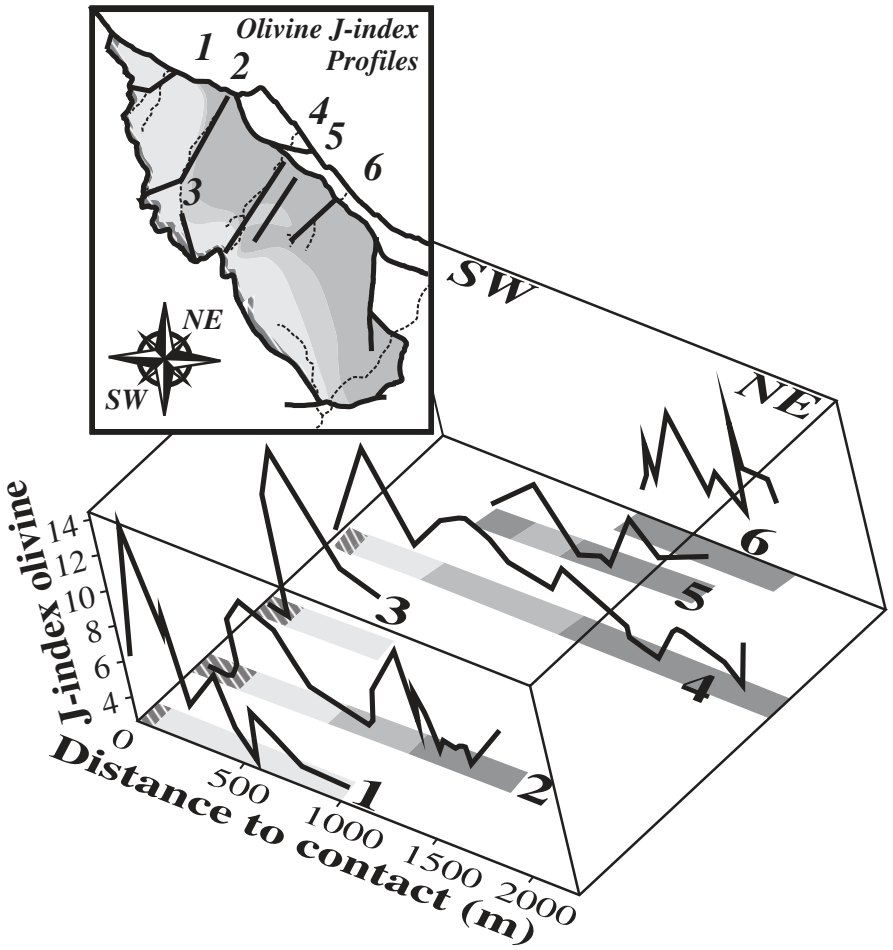

Fig. 16. Evolution of the olivine CPO strength, characterized by the J-index, as a function of the distance to the contact with the crustal units, along six profiles normal to the structure of the massif. Inset shows the location of the profiles.

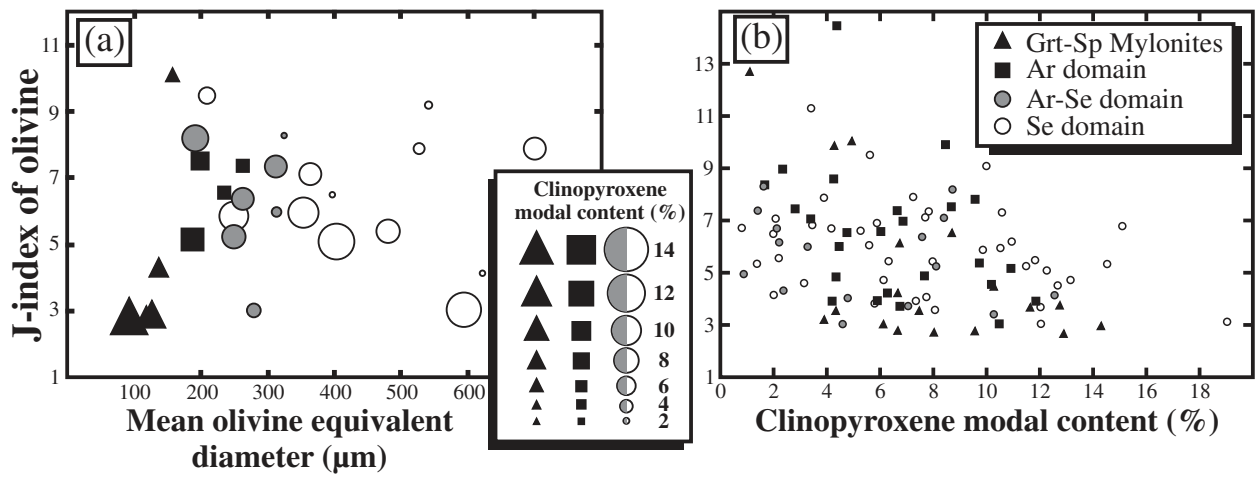

Fig. 17. (a) Olivine CPO strength, characterized by the J-index, as a function of the mean olivine 2D equivalent diameter and of the modal content of clinopyroxene (proportional to the size of the symbol) in samples for which grain size analysis was performed. (See text for explanation.) (b) Olivine CPO strength as a function of the clinopyroxene modal content for all analysed samples.

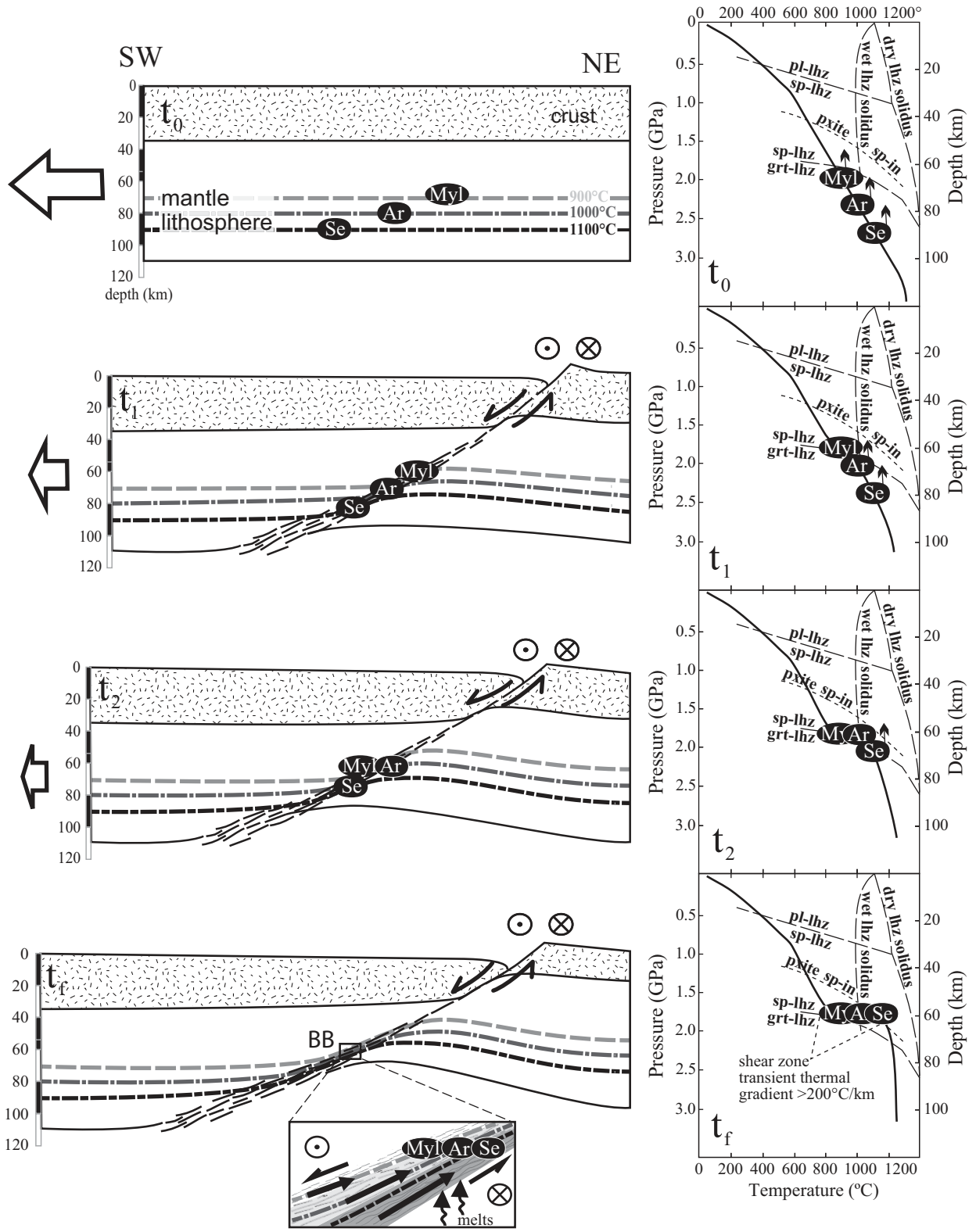

Fig. 18. Two-dimensional model of the relation between shearing and evolution of *P–T* conditions in the various tectono-metamorphic domains in the Beni Bousera shear zone. Left: schematic illustrations of the vertical component of displacement in the shear zone; the horizontal component of displacement is represented only by left-lateral shearing symbols. Right: *P–T* history in the tectono-metamorphic domains. At t_0, the Grt–Sp mylonites ('Myl'), Ar ('Ar') and Se domains ('Se') are at different, increasing *P–T* conditions along the same geotherm, which

(continued)

An alternative explanation for the interpenetrating olivine–orthopyroxene grain boundaries is solid-state silica exchange reactions induced by deformation in a diffusion-accommodated grain boundary sliding regime, as observed in experiments in very fine-grained olivine–orthopyroxene aggregates (Sundberg & Cooper, 2008). However, the grain sizes in the experiments are more than one order of magnitude smaller than in the Beni Bousera mylonites, and the temperatures are much higher, resulting in much lower stresses. The olivine CPO also differs as the experimental samples showed an alignment of [001] in the shear direction that is not observed in the Beni Bousera Grt–Sp mylonites (Fig. 14).

The Ar domain peridotites: deformation under increasing temperature conditions

Microstructures (Fig. 11a–c) and CPO (Fig. 14) also point to deformation by dislocation creep in the Ar domain, with dominant activation of the [100](010) slip system in olivine and of [001]{110} in the pyroxenes. The continuous textural evolution from fine-grained porphyroclastic peridotites at the contact with Grt–Sp mylonites to medium-grained porphyroclastic peridotites at the Ar–Se transition (the olivine mean and recrystallized grain sizes increase and the volume fraction of recrystallized grains decreases; Figs 8 and 9) suggests decreasing plastic work rates owing to decreasing stresses, a more distributed deformation resulting in lower strain rates, or both. This evolution is consistent with the increase in equilibration temperatures within this domain (900–1000°C; Fig. 14). Boudinage and folding of the more competent garnet pyroxenite layers indicate high finite strains, but the intensity of the deformation of the pyroxenites is variable; strongly boudinaged pyroxenites alternate with almost undeformed ones. Lower finite strains towards the Ar–Se domain are suggested by the decrease in olivine CPO intensity (Fig. 16).

Less extensive recrystallization, indicated by the increase in the area fraction occupied by porphyroclasts (Fig. 9c), may account for the strong olivine CPO observed in the Ar domain (Fig. 16). Less extensive recrystallization and/or deformation under higher temperature–lower stress conditions may also explain the change in olivine CPO symmetry: although axial-[010] still predominates, some Ar domain peridotites display orthorhombic or axial-[100] patterns (Fig. 15). As in the Grt–Sp mylonites, the CPOs of the pyroxenes do not show a dispersion of [001] in the foliation plane (Fig. 14) that could be interpreted as indicating a transpressive deformation regime.

Finally, the irregular shape of orthopyroxene porphyroclasts, which show embayments, often elongated parallel to the foliation, filled by olivine in structural continuity with matrix crystals (Fig. 11b and c), suggests some late to post-kinematic reactive melt percolation, leading to crystallization of olivine at the expense of orthopyroxene in this domain.

The Ar–Se transition and the Se domain: deformation under very high temperature conditions, near the peridotite solidus

The most remarkable feature of Ar–Se peridotites is the centimetre-scale olivine crystals elongated parallel to the lineation, with lobate grain boundaries (Fig. 9d–f). The transition from the Ar–Se to the Se domain is characterized by an additional grain coarsening (Fig. 8) and widespread sinuous grain boundaries. In both domains, undulose extinction, subgrains in olivine, and kinks in pyroxenes are ubiquitous (Figs 11d, e and 12). The above association of microstructures is characteristic of an association of dislocation creep and extensive synkinematic grain boundary migration, suggesting deformation under high-temperature, near-solidus conditions. This is consistent with the very high equilibration temperatures recorded in some peridotites (>1200°C, Fig. 13) from both domains and in garnet–spinel pyroxenites from the Ar–Se domain ($T > 1100$°C, $P = 1{\cdot}8$ GPa; Frets *et al.*, 2012). The more widespread character of the grain boundary migration in the Se domain suggests higher temperatures or low melt fractions present during deformation.

Synkinematic reactive melt percolation in the Se domain is suggested by the abundant dunites and spinel websterites, which form layers or lenses with diffuse boundaries parallel or at a low angle to the peridotite foliation (Fig. 7). It is also suggested by petrographic observations indicating crystallization of olivine at the expense of

Fig. 18 Continued
corresponds to a thermally equilibrated 100 km thick continental lithosphere with an initially 35 km thick crust (arbitrary choice). The initial geotherm was calculated considering surface and basal heat flows of 65 and 30 mW m^{-2} and thermal conductivity values for the crust and the mantle of 2·50 and 3·35 W m^{-1}°C^{-1}, respectively. At t_1, shearing resulted in upwelling and near-isothermal decompression of all domains; at this stage the Grt–Sp mylonites reached 60 km depth. Juxtaposition of progressively hotter domains across the shear zone led to migration of the deformation towards its lower and hotter parts and addition of the cold domains to the hanging wall (the Grt–Sp mylonites, at this stage). This evolution continued until upwelling of the Se domain to *c.* 60 km allowed for decompression melting in the Se. Inset shows this final stage (t_f), which is recorded in the Beni Bousera peridotite. Myl, Grt–Sp mylonites; Ar, Ariegite domain; Se, Seiland domain. The crust is shown for the sake of completeness of the lithosphere section, but constraints from the *P–T–t* evolution in the crustal units of the Sebtides were not included in the model. Dry and wet lherzolite solidi are from Takahashi & Kushiro (1983) and Kushiro *et al.* (1968), respectively. Spinel–plagioglase reaction in lherzolites is from Green & Ringwood (1967). Spinel–garnet reaction is based on the geobarometer calibration in the CMAS–Cr system (Webb & Wood, 1986) corrected for the effect of FeO in olivine (O'Neill, 1981) using the mineral compositions of garnet–spinel mylonite BB001W (not shown). Sp-in curve for Beni Bousera pyroxenites is from Frets *et al.* (2012).

orthopyroxene (dunite-forming reactions) in both the Ar–Se and Se domains (Fig. 11c and e). Moreover, the bimodal CPO of the pyroxenes, where one texture component, usually the strongest one, is correlated with the olivine CPO, but the other, which is characterized by an [001] maximum at a high angle to the lineation, is non-correlated (Fig. 14), implies late crystallization (relative to the deformation) of some of the ortho- and clinopyroxene in the peridotites of the Se and Ar–Se domains. The higher proportion of non-correlated pyroxene CPO in the Ar–Se domain relative to the Se domain may suggest a difference in the timing of melt percolation relative to the deformation: syn- to late kinematic in the Se domain and late to post-kinematic in the Ar–Se domain. Melting might have been triggered by decompression during deformation, which is suggested by the occurrence of weakly deformed spinel–pyroxene pseudomorphs of garnet (Fig. 12d). The occurrence of both dunite-forming and refertilization reactions may be explained by spatio-temporal variations in the degree of Si saturation of the percolating melts, leading to either pyroxene dissolution or crystallization (e.g. Berger & Weber, 1991; Kelemen *et al.*, 1992; Garrido & Bodinier, 1999; Lenoir *et al.*, 2001; Tommasi *et al.*, 2004; Le Roux *et al.*, 2007).

Extensive grain growth, which reinforced the volume of the texture components representing the coarse crystals, may account for marked strengthening of the olivine CPO at the transition from the Ar to the Ar–Se domain (Fig. 16). A similar interpretation was proposed to explain the strong olivine CPO in coarse-grained peridotites from the Ronda recrystallization front (Vauchez & Garrido, 2001). This domain is also characterized by a higher proportion of orthorhombic olivine CPO (Fig. 14), consistent with effective grain boundary migration counteracting the dispersion of [100] produced by subgrain rotation recrystallization (Falus *et al.*, 2011). On the other hand, variations in the instantaneous melt fraction during deformation, which cannot be inferred from the present modal composition, might explain the high variability of the olivine CPO intensity and symmetry in the Se domain (Fig. 14). Small melt or fluid fractions at triple junctions and along grain boundaries reduce the contact area between grains, locally enhancing stresses and favouring dislocation creep and CPO development (Hirth & Köhlstedt, 1995*a*). High instantaneous melt fractions, however, favour diffusion, leading to a lower contribution of dislocation creep to the deformation (Hirth & Köhlstedt, 1995*b*) and to a decrease of the CPO intensity (Holtzman *et al.*, 2003; Le Roux *et al.*, 2008). A similar interpretation was proposed to account for the variability in olivine CPO intensity in lherzolites from the Ronda peridotite massif (Soustelle *et al.*, 2009). In addition, the strong axial-[100] patterns that characterize some dunitic layers are consistent with recent observations in the uppermost mantle section of the Oman ophiolite, which highlighted a change in olivine CPO symmetry from axial-[100] to axial-[010] between dunitic and more gabbroic layers, interpreted as recording a change in deformation mode controlled by the synkinematic melt fraction (Higgie & Tommasi, 2012).

Together, these data point to deformation in the presence of variable melt fractions in the Se domain. Within this framework, the four small (<200 m wide) domains with vertical foliations (Figs 2 and 3) in the upper part of the Se domain might represent small gravitational instabilities (diapirs) formed in response to local melt accumulation, suggested by the higher abundance of products of melt–peridotite reaction (i.e. dunite and diffuse websterite layers) in their vicinity. This interpretation is corroborated by (1) the very localized nature of these vertical lineation domains, (2) the sharp reorientation of the foliation and lineation at their boundaries (over 10–20 m), and (3) their isometric exposures, which suggest a circular cross-section in a plane normal to the flow direction. The association with reactive melt percolation products and the sharp reorientation of the lineation and foliation are indeed reminiscent of structures mapped at the kilometre scale in the mantle section of the Oman ophiolite and interpreted as diapiric upwellings beneath an active ridge (Jousselin *et al.*, 1998). The latter have, however, larger dimensions (kilometre scale) than the present ones (100–200 m).

The Beni Bousera peridotite massif: a low-angle, oblique-slip shear zone accommodating mantle exhumation during lithospheric thinning

Any model of the evolution of the Beni Bousera massif must account for the three major results of the present study, which are as follows.

(1) The consistency of the orientation of the foliations and lineations across the massif (except for the small areas with vertical lineations), the lack of cross-cutting structural relations, and the continuity in the evolution of deformation conditions recorded by microstructures and CPO, which indicate that all structures and metamorphic assemblages in the Beni Bousera massif were produced by a single tectonic event with consistent kinematics.

(2) The petrological–structural analysis performed in this study, together with previous data on the associated pyroxenites (Frets *et al.*, 2012), constrains that (a) equilibration occurred at increasing temperature and decreasing pressure from the Grt–Sp mylonites (850–900°C, 2 GPa) to the Se domain (≥1200°C and 1·8 GPa) and (b) the P–T equilibrium conditions in the different domains are syn- to late kinematic.

(3) Structural mapping shows that lineations in the mylonites, the Ar and the Ar–Se domains are dominantly subparallel to the limits of the tectono-metamorphic

domains and that they become oblique to the latter in the Se domain (Figs 2 and 3). The dominant tectonic transport was therefore at a high angle to the projection of the metamorphic gradient on the present topographic surface, which records the vertical displacement. In addition, although observations are rare, shear-sense indicators imply a component of simple shear with a dominantly top-to-the-SE displacement.

All these constraints may be accounted for if the entire Beni Bousera massif represents a shear zone, which accommodated exhumation of the mantle lithosphere. If the small areas with vertical lineations in the Se domain represent, as proposed here, small diapirs, these lineations mark the palaeo-vertical and preclude any late rotation around non-vertical axes. Rigid rotations around a vertical axis, as suggested by palaeomagnetic data (74° anticlockwise; Saddiqi *et al.*, 1995), might have occurred during the emplacement of the massif in the crust or later, but such rotations cannot orient the lineation along the foliation dip, implying that the shear zone had an oblique-slip vector. The simplest interpretation is then to consider that the current orientation of the ductile structures and of the petrological–structural zoning of the massif is similar to its initial orientation in the mantle. This assumption is corroborated by the consistency in the orientation of the ductile lineations in the Beni Bousera peridotites and in the overlying crustal units, which are all parallel to the trend of the belt (Figs 1 and 2). Orogen-parallel lineations were also described in the Melilla area (Negro, 2005) about 170 km east of the Beni Bousera massif. This suggests that, if any rigid rotation occurred, it happened at a late stage and affected the entire margin.

In this framework, the Beni Bousera peridotite is a low-angle, oblique-slip, shear zone that accommodated simultaneously a belt-parallel displacement component and thinning of the mantle lithosphere. The Grt–Sp mylonites and the Se domain constituted, respectively, the upper and the lower part of this mantle shear zone. Stretching in multiple directions within such an oblique-slip shear plane may have contributed, together with dynamic recrystallization, to the predominance of axial-[010] olivine CPO, because such a deformation induces dispersion of [100] in the foliation plane (Tommasi *et al.*, 1999). The gradual reorientation and dispersion of the lineation in the Se domain might indicate some strain partitioning in the hotter and hence more ductile levels of the shear zone, leading to a redistribution of deformation with lower finite strains, lower finite strains in this domain, or a change in kinematics at the base of the lithospheric section, suggesting partial coupling to the deformation in the underlying asthenospheric mantle (clutch tectonics; Tikoff *et al.*, 2004).

Figure 18 illustrates the proposed evolution of the Beni Bousera shear zone, focusing on the vertical displacement component, which is well constrained by the metamorphic record. The shear zone has been tentatively extended to the crust for consistency; however, the sketch does not necessarily reflect the actual tectonic evolution of the overlying crustal units. As by definition a shear zone implies a displacement between the blocks it separates, the four tectono-metamorphic domains that are at present in continuity in the Beni Bousera massif must have originated at different locations. For the sake of simplicity and because the available data (this study; Tabit *et al.*, 1997; Afiri *et al.*, 2011; Frets *et al.*, 2012) do not allow us precisely to constrain the initial P–T conditions in the various domains, we propose that the four tectono-metamorphic domains, from the Grt–Sp mylonites to the Se domain, were initially equilibrated at progressively deeper levels along the same geotherm (Fig. 18, t_0). This assumption differs strongly from previous models for Betic–Rifean peridotites, which assumed that the various domains equilibrated at the same primary P–T conditions (Obata, 1980; Van der Wal & Vissers, 1993; Garrido *et al.*, 2011; Lenoir *et al.*, 2001). This previous assumption is, however, impossible to reconcile with the results of the present study: as the shear zone accommodates a vertical displacement (even if it is not the sole displacement component), the various domains must have originated at different depths.

We propose therefore that the Beni Bousera shear zone resulted in tectonic juxtaposition—in strong thermal disequilibrium—of units derived from initially different lithospheric levels, becoming no longer tectonically active at a final depth of ~60 km (1·8 GPa; Fig. 18, t_f). The initially deeper and hotter levels, represented by the Se domain, underwent the largest displacement. This implies that the apparently less strained Se peridotites accommodated higher displacements than the fine-porphyroclastic peridotites from the Ar domain and the Grt–Sp mylonites. This apparent contradiction may indicate a higher strain localization in the colder parts of the shear zone. Although the limits of the shear zone are not exposed in the Beni Bousera massif, more localized deformation in the Grt–Sp mylonites is consistent with the smaller present-day thickness of this domain.

Fast shearing avoided significant thermal re-equilibration by conduction. Deeper domains were juxtaposed by nearly adiabatic decompression at their primary temperature conditions (Fig. 18, right column). This led to gradual migration of the deformation from the shallower and colder Grt–Sp mylonites domain towards the progressively hotter Ar, Ar–Se, and finally Se domains, with the colder domains being successively added to the hanging wall (Fig. 18, $t_1 - t_f$). Slow thermal conduction (relative to displacement rates) and cessation of the deformation allowed the preservation of metastable HP assemblages in the cold

Grt–Sp mylonites domain. The preservation of the metastable HP assemblages in the Grt–Sp mylonites domain was also favoured by sluggish reaction kinetics owing to the low temperatures. In contrast, in the hotter Se domain, faster reaction kinetics erased most of the petrological record of earlier HP assemblages (only locally preserved as opx–cpx–sp symplectites; Fig. 12d). Microstructural evidence for melt-present deformation in the Se domain indicates that these peridotites probably crossed the lherzolite wet solidus upon decompression (Fig. 18, right column, t_f).

This dynamic scenario satisfactorily accounts for the large apparent thermal (~250°C) and pressure difference (at least 0·5 GPa) recorded at present in a mantle section barely 2 km thick (Fig. 18, t_f) and for partial melting in the Se domain without need of an extrinsic and exotic heat source as previously proposed for the Ronda peridotite (Van der Wal & Vissers, 1993, 1996; Garrido & Bodinier, 1999; Lenoir *et al.*, 2001; Soustelle *et al.*, 2009). The strong anisotropy of thermal diffusivity of upper mantle rocks may have contributed to the preservation of a high temperature gradient within the shear zone, because in a deformed peridotite thermal diffusion in a direction normal to the shear plane is slower by 30% than in a non-deformed rock (Tommasi *et al.*, 2001). Latent heat sink effects during partial melting in the Se domain may also have hindered thermal equilibration.

Despite these effects, one may use thermal re-equilibration constraints to roughly estimate strain rates in the shear zone. Evidence for partial thermal re-equilibration in Beni Bousera, such as static garnet–spinel transformation in pyroxenites in the Ar–Se domain (Frets *et al.*, 2012), is limited to <1 km. Considering a thermal diffusivity of $5 \times 10^{-7}\,m^2\,s^{-1}$ (diffusion in a direction normal to the foliation at temperatures of 900°C; Tommasi *et al.*, 2001), thermal equilibrium over a distance of 1 km should be reached in *c.* 60 kyr. The magnitude of the displacement on the shear zone can be estimated on the basis of the estimated vertical displacement and the orientation of the foliation and lineation. Considering an end-member case, in which all decompression from 90 to 60 km depth is accommodated by the Beni Bousera shear zone, and the present-day orientation of the foliation and lineation, the maximum displacement in the shear zone is *c.* 120 km. Strain rates must then be higher than $10^{-11}\,s^{-1}$ to avoid conductive re-equilibration at the kilometre scale. Such high strain rates are consistent with extremely rapid exhumation and cooling rates of the overlying crustal units (*c.* 3 km Ma^{-1} and 250–450°C Ma^{-1}; Haissen *et al.*, 2004). Moreover, given the rather fast thermal re-equilibration at the kilometre scale (*c.* 60 kyr), to preserve the metastable tectono-metamorphic zoning observed in the Beni Bousera peridotite further exhumation must have occurred shortly after the juxtaposition of the four domains. However, this tectonic episode is not recorded within the Beni Bousera massif.

Comparison with previous models and consequences for the evolution of the Betic–Rif system

A wealth of tectonic models has been proposed for the exhumation and intra-crustal emplacement of the Rif and Betic mantle peridotites. Based on the structures in the peridotites and associated crustal rocks, exhumation of the subcontinental mantle lithosphere has been attributed to pure extension (Platt *et al.*, 2006), deformation in transcurrent or transpressional shear zones (Tubía, 1994; Tubía *et al.*, 2004), or alternating contractional and extensional processes related to continental subduction followed by extension (Balanyá *et al.*, 1997). However, all of these models failed to explain the petrological–structural zoning of the peridotites, which implies deformation under decreasing pressure and increasing temperature conditions. Other models focused on this aspect (Obata, 1980; Van der Wal & Vissers, 1993, 1996; Précigout *et al.*, 2007; Afiri *et al.*, 2011; Garrido *et al.*, 2011). Obata (1980) proposed that the petrological zoning of the Ronda peridotite was formed during progressive inward cooling of an upwelling mantle diapir. More recent models (Précigout *et al.*, 2007; Afiri *et al.*, 2011) have proposed that lithospheric-scale extensional shear zones accommodated the exhumation of the Ronda and Beni Bousera peridotites. However, these studies focused on the mylonites and dismissed the lack of discontinuity in both the tectonic and metamorphic records within the peridotites, failing to recognize that the entire peridotite massif records the functioning of a single shear zone.

Another common thread of the previous tectonic and petrological models for the evolution of the Betic–Rif peridotites (Kornprobst, 1970; Obata, 1980; Kornprobst *et al.*, 1990; Van der Wal & Vissers, 1993; Tabit *et al.*, 1997; Précigout *et al.*, 2007; Afiri *et al.*, 2011; Garrido *et al.*, 2011) is that the various tectono-metamorphic domains were considered as originating at similar HP–HT pre-kinematic ('primary') conditions. This P–T–t evolution requires sequential overprinting of the earliest HP–LT structures upon decompression and heating (Van der Wal & Vissers, 1993, 1996; Van der Wal & Bodinier, 1996; Lenoir *et al.*, 2001; Soustelle *et al.*, 2009; Afiri *et al.*, 2011). Such an evolution is not thermally realistic, because it requires a heat sink on top of the peridotites for development of garnet–spinel mylonites by cooling and decompression, as well as heating and decompression by an extrinsic (unknown) heat source at the base of the massif to generate the HT–LP partially melted Se domain. In addition, the extreme thermal gradient implied by the preservation of HP–LT assemblages in garnet–spinel mylonites less than 1 km from

the melting front ($125^{\circ}C\,km^{-1}$) is incompatible with simple conductive heating.

The present model solves these problems. It consistently accounts for the observed metamorphic evolution in both Beni Bousera and Ronda peridotites, as high strain rates in a low-angle shear zone may account for fast exhumation of the subcontinental mantle lithosphere, allowing for development of a very strong transient thermal gradient across the shear zone and partial melting by decompression in the hotter and initially deeper parts of the shear zone. It is also fully consistent with the continuity in the microstructural and equilibrium temperature conditions in the peridotite massifs.

The observed structures in Beni Bousera, however, cannot account for the emplacement of the massif into the crust; this massif records only the earlier stages of mantle lithospheric exhumation from the garnet to the spinel lherzolite facies. Lu–Hf ages in garnet clinopyroxenites from the Grt–Sp mylonites and Ar domain in Beni Bousera suggest that these domains were cooled to <850°C by 24 ± 3 Ma (Pearson & Nowell, 2004). These ages allow correlation of the tectono-metamorphic evolution recorded in the Beni Bousera peridotite with the earliest stages of extension of the proto-Alboran lithospheric mantle, probably in response to slab retreat. Based on structural mapping of the Ronda plagioclase-facies tectonites, a low-pressure facies not exposed in the Beni Bousera massif, Hidas *et al.* (2012) proposed that final exhumation and emplacement of the peridotites in the crust occurred by lithospheric scale folding and thrusting during inversion of the back-arc rift owing to the collision of the retreating slab with the Algerian margin during the late Oligocene (21–23 Ma); that is, shortly after the cessation of the shearing in the Beni Bousera shear zone. This short time interval between the functioning of the shear zone and the final exhumation of the massif is consistent with the preservation of the metastable thermal gradient produced by the shearing.

Finally, although the present-day orientation of the lineation in all internal units of the Rif belt may have been affected by rigid rotations, it is noteworthy that the ductile lineations in the crustal units in the Sebtides (Fig. 1) are also systematically normal to the projected metamorphic gradient recorded by these units (Loomis, 1972; Janots *et al.*, 2006; Negro *et al.*, 2006), suggesting that crustal thinning was also accompanied by a dominant belt-parallel displacement, which has up to now been largely ignored. At the belt scale, such oblique-slip shear zones will produce horizontal shearing and vertical thinning; that is, a transtensional deformation of the continental margin. Such deformation of the mantle lithosphere will produce belt-parallel fast shear-wave polarizations, such as those observed in the Betic–Rif system (Buontempo *et al.*, 2008). Rift-parallel fast shear-wave polarizations are observed in many active rifts (e.g. the East African and Rio Grande rifts; e.g. Sandvol *et al.*, 1992; Kendall *et al.*, 2005), suggesting that oblique-slip shear zones may be a general feature accommodating thinning of the subcontinental lithospheric mantle.

CONCLUSIONS

Structural mapping and analysis of microstructures, CPO and equilibration conditions allow the definition of four tectono-metamorphic domains in the Beni Bousera peridotite massif, which are from top to bottom: the Grt–Sp mylonites, the Ariegite domain, the Ariegite–Seiland transition, and the Se domains. These domains are characterized by consistent kinematics, recorded by dominant shallow SW-dipping foliations with SE–NW-striking lineations that rotate gradually towards a south–north to SSW–NNE strike in the Se domain. Our data also highlight a continuous gradient in the microstructures and pressure and temperature equilibration conditions and the absence of any crosscutting relationships, except for four small zones (<200 m wide) with vertical lineations in the Se domain.

The microstructures and well-developed CPO of the peridotites support deformation dominantly by dislocation creep in all domains. The increase in average olivine grain sizes and decrease in the volume fractions of recrystallized grains from the Grt–Sp mylonites to the Se domain indicate, however, decreasing plastic work rates. This evolution is consistent with petrological data, which signal an increase in synkinematic temperatures and decrease in synkinematic pressures from Grt–Sp mylonites (900°C, 2·0 GPa) to the Seiland domain (1150°C, 1·8 GPa). The gradual change in olivine CPO pattern, from a dominantly axial-[010] symmetry in the mylonites and Ar domain to a more orthorhombic symmetry in the Se domain, is also consistent with increasing synkinematic temperature conditions. Extensive dynamic recrystallization owing to deformation under high stress and strain rates may have produced the dispersion of [100] axes in the Grt–Sp mylonites and Ar domain, whereas high synkinematic temperatures allowed for fast grain boundary migration and growth, favouring the development of orthorhombic olivine CPO patterns in the Ar–Se and Se domains. The diffuse dunite–websterite layering subparallel to the foliation and extensive microstructural evidence for syn- to late kinematic reactive melt percolation indeed imply deformation under near-solidus conditions in the Se domain. The overall predominance of axial-[010] patterns in the Beni Bousera peridotites may, however, also record a 3D deformation regime with multiple stretching directions within the shear plane.

Based on these observations, we propose that the Beni Bousera peridotite massif is an oblique-slip shear zone, which accommodated the exhumation of the mantle

lithosphere by up to *c.* 60 km. Fast advection of deep and hot peridotites in response to high strain rates in the shear zone allowed development of a very high transient temperature gradient (~125°C km^{-1}), which resulted in the migration of the deformation towards the lower and hotter parts of the shear zone, allowing for preservation of the low-temperature deformation structures and of metastable HP assemblages in the colder domains, which were progressively accreted to the shear zone hanging wall. In this original model—this is the first time that it is recognized that the entire peridotite massif forms the shear zone—no external heat source is needed to account for partial melting in the Se domain, which may be explained by near-isothermal decompression in response to shearing allowing the wet lherzolite solidus to be crossed. The localized vertical lineations in the Se domain may then be explained as recording small (<200 m wide) diapirs in response to local melt accumulation, constraining that the shear zone was shallowly dipping (<30°) in the mantle.

Although the orientation of the lineations during shearing in the mantle cannot be uniquely constrained, if the vertical lineation domains represent diapirs they record the palaeo-vertical. In addition, the consistent orientation of the ductile lineations in both the Beni Bousera peridotites and the overlying crustal units parallel to the trend of the belt does not allow for solid body rotation of the peridotites relative to the crustal units of the internal domains of the Rif belt. The simplest model is then to interpret the current orientation of the ductile structures in Beni Bousera as similar to its original orientation in the mantle. In this case, the Beni Bousera peridotite is a low-angle oblique-slip shear zone, which accommodated simultaneously belt-parallel displacement and thinning of the mantle lithosphere. Such a deformation can be understood in geodynamic terms as a transtensional deformation of the margin in response to the slab retreat.

ACKNOWLEDGEMENTS

E.C.F. warmly thanks all the participants of the four field missions in Beni Bousera and in particular our Moroccan colleagues for their hospitality during these campaigns. E.C.F. is also grateful to the Montpellier team for support during his not-so-short-stays for EBSD measurements. We thank R. Reyes-González, C. Nevado and D. Delmas for providing high-quality thin sections for EBSD measurements, and A. Delplanque for computer drawing the cross-sections.

FUNDING

This research benefited from several grants and fellowships funded by the European Fund of Regional Development. The research leading to these results has been funded by Crystal2Plate, an EU-FP7 Marie Curie Action under grant agreement PITN-GA-2008-215353. This work was also supported by the International Lithosphere Program (grant CC4-MEDYNA to C.J.G.), the Spanish Ministry of Economy and Competitiveness (MICINN) (grant CGL2010-14848 to C.J.G.), the Junta de Andalucía (grants RNM-131 and 2009RNM4495 to C.J.G.).

SUPPLEMENTARY DATA

Supplementary data for this paper are available at *Journal of Petrology* online.

REFERENCES

Afiri, A., Gueydan, F, Pitra, P., Essaifi, A. & Précigout, J. (2011). Oligo-Miocene exhumation of the Beni-Bousera peridotite through a lithosphere-scale extensional shear zone. *Geodinamica Acta* **24**(1), 49–60.

Austin, N. & Evans, B. (2007). Paleowattmeters: a scaling relation for dynamically recrystallized grain size. *Geology* **35**, 343–346.

Bachmann, F., Hielscher, R. & Schaeben, H. (2010). Texture analysis with MTEX—free and open source software toolbox. *Solid State Phenomena* **160**, 63–68.

Balanyá, J. C., García-Dueñas, V., Azañón, J. M. & Sánchez-Gómez, M. (1997). Alternating contractional and extensional events in the Alpujarride Nappes of the Alboran domain (Betics, Gibraltar arc). *Tectonics* **16**, 226–238, doi:10.1029/96TC03871.

Bascou, J., Tommasi, A. & Mainprice, D. (2002). Plastic deformation and development of clinopyroxene lattice preferred orientations in eclogites. *Journal of Structural Geology* **24**, 1357–1368.

Ben Ismail, W. & Mainprice, D. (1998). An olivine fabric database: an overview of upper mantle fabrics and seismic anisotropy. *Tectonophysics* **296**, 145–158.

Berger, E. T. & Weber, B. C. (1991). Dunitification of mantle lithosphere below the Society Archipelago: Evidence for magma–mantle thermal and chemical transfers through xenoliths from the Papenoo valley, Tahiti. *Journal of Geodynamics* **13**, 221–252.

Bouybaouène, M. L., Michard, A. & Goffé, B. (1998). High-pressure granulites on top of the Beni Bousera pridotites, Rif Belt, Morocco: a record of an ancient thickened crust in the Alboran domain. *Bulletin de la Societé Géologique de France* **2**, 153–162.

Brace, W. F. & Köhlstedt, D. L. (1980). Limits on lithospheric stress imposed by laboratory experiments. *Journal of Geophysical Research* **85**, 6248–6252.

Brey, G. P. & Köhler, T. (1990). Geothermobarometry in four-phase lherzolites. 2. New thermobarometers, and practical assessment of existing thermobarometers. *Journal of Petrology* **31**, 1353–1378.

Bunge, H. J. (1982). *Texture Analysis in Materials Sciences*. Butterworth.

Buontempo, L., Bokelmann, G. H. R., Barruol, G. & Morales, J. (2008). Seismic anisotropy beneath southern Iberia from SKS splitting. *Earth and Planetary Science Letters* **273**, 237–250.

Burchfiel, B. C., Chen, Z., Hodges, K. V., Liu, Y., Royden, L. H., Deng, C. & Xu, J. (1992). *The South Tibetan Detachment System, Himalayan orogen: Extension Contemporaneous with and Parallel to Shortening in a Collisional Mountain Belt. Geological Society of America, Special Papers* **269**, 41 pp.

Bystricky, M., Kuntze, K., Burlini, L. & Burg, J.-P. (2000). High shear strain of olivine aggregates: rheological and seismic consequences. *Science* **290**, 1564–1567.

Chalouan, A. & Michard, A. (1990). The Ghomarides nappes, Rif coastal Range, Morocco: a Variscan chip in the Alpine belt. *Tectonics* **9**, 1565–1583.

Chalouan, A., Michard, A., El Kadiri, K., Negro, F., Frizon de Lamotte, D. & Saddiqi, O. (2008). The Rif Belt. In: Michard, A., Chalouan, A., Saddiqi, O. & Frizon de Lamotte, D. (eds) *Continental Evolution: The Geology of Morocco*. Springer, pp. 203–302.

Demouchy, S., Tommasi, A., Balaran, T. B. & Cordier, P. (2013). Low strength of Earth's uppermost mantle inferred from tri-axial deformation experiments on dry olivine crystals. *Physics of the Earth and Planetary Interiors* **220**, 37–49.

Dijkstra, A., Drury, M., Vissers, R., Newman, J. & Van Roermund, H. (2004). Shear zones in the upper mantle: Evidence from alpine- and ophiolite-type peridotite massifs. In: Alsop, I. & Holdsworth, R. E. (eds) *Flow Processes in Faults and Shear Zones. Geological Society, London, Special Publications* **224**, 11–24.

Durham, W. B. & Goetze, C. (1977). Plastic flow of oriented single crystals of olivine: 1. Mechanical data. *Journal of Geophysical Research* **82**, 5755–5770.

El Atrassi, F., Brunet, F., Bouybaouene, M., Chopin, C. & Chazot, G. (2011). Melting textures and microdiamonds preserved in graphite pseudomorphs from the Beni Bousera peridotite massif, Morocco. *European Journal of Mineralogy* **23**(2), 157–168, doi:10.1127/0935-1221/2011/0023-2094.

England, P. C. (1983). Constraints on extension of continental lithosphere. *Journal of Geophysical Research* **88**, 1145–1152.

Falus, G., Tommasi, A. & Soustelle, V. (2011). Effect of dynamic recrystallization on olivine crystal preferred orientations in mantle xenoliths deformed under varied stress conditions. *Journal of Structural Geology* **33**, 1528–1540, doi:10.1016/j.jsg.2011.09.010.

Frets, E., Tommasi, A., Garrido, C. J., Padrón-Navarta, J. A., Amri, I. & Targuisti, K. (2012). Deformation processes and rheology of pyroxenites under lithospheric mantle conditions. *Journal of Structural Geology* **39**, 138–157, doi:10.1016/j.jsg.2012.02.019.

Garrido, C. J. & Bodinier, J.-L. (1999). Diversity of mafic rocks in the Ronda peridotite: evidence for pervasive melt/rock reaction during heating of subcontinental lithosphere by upwelling asthenosphere. *Journal of Petrology* **40**, 729–754.

Garrido, C. J., Kelemen, P. B. & Hirth, G. (2001). Variation of cooling rate with depth in lower crust formed at an oceanic spreading ridge: Plagioclase crystal size distributions in gabbros from the Oman ophiolite. *Geochemistry, Geophysics, Geosystems* **2**, 1041, doi:10.1029/2000GC000136.

Garrido, C. J., Gueydan, F., Booth-Rea, G., Precigout, J., Hidas, K., Padrón-Navarta, J. A. & Marchesi, C. (2011). Garnet lherzolite and garnet–spinel mylonite in the Ronda peridotite: Vestiges of Oligocene backarc mantle lithospheric extension in the western Mediterranean. *Geology* **39**, 927–930, doi:10.1130/G31760.1.

Green, D. H. & Ringwood, A. E. (1967). The stability fields of aluminous pyroxene peridotite and garnet peridotite. *Earth and Planetary Science Letters* **3**, 151–160.

Gueddari, K., Piboule, M. & Amossé, J. (1996). Differentiation of platinum-group elements (PGE) and of gold during partial melting of peridotites in the lherzolitic massifs of the Betico-Rifean range (Ronda and Beni Bousera). *Chemical Geology* **134**, 181–197.

Gysi, A. P., Jagoutz, O., Schmidt, M. W. & Targuisti, K. (2011). Petrogenesis of pyroxenites and melt infiltrations in the ultramafic complex of Beni Bousera, Northern Morocco. *Journal of Petrology* **52**, 1679–1735.

Haissen, F., García-Casco, A., Torres-Roldan, R. L. & Aghzer, A. M. (2004). Decompression reactions and *P–T* conditions in high-pressure granulites from Casares–Los Reales units of the Betic–Rif belt (S Spain and N Morocco). *Journal of African Earth Sciences* **39**, 375–383.

Hidas, K., Booth-Rea, G., Garrido, C. J., Martínez- Martínez, J. M., Padrón-Navarta, J. A., Giaconia, F., Frets, E. & Marchesi, C. (2012). Backarc basin inversion and subcontinental mantle intracrustal emplacement: Kilometre-scale folding and shearing at the base of the proto-Alborán lithospheric mantle (Betic cordillera, South Spain). *Journal of the Geological Society, London* **170**, 45–55.

Hielscher, R. & Schaeben, H. (2008). A novel pole figure inversion method: specification of the MTEX algorithm. *Journal of Applied Crystallography* **41**, 1024–1037.

Higgie, K. & Tommasi, A. (2012). Feedbacks between deformation and melt distribution in the crust–mantle transition zone of the Oman ophiolite. *Earth and Planetary Science Letters* **359–360**, 61–72.

Higgins, M. D. (1994). Numerical modeling of crystal shapes in thin-sections: estimation of crystal habit and true sizes. *American Mineralogist* **79**, 113–119.

Hirth, G. & Köhlstedt, D. L. (1995*a*). Experimental constraints on the dynamics of the partially molten upper mantle 2. Deformation in the dislocation creep regime. *Journal of Geophysical Research* **100**(B8), 15441–15449.

Hirth, G. & Köhlstedt, D. L. (1995*b*). Experimental constraints on the dynamics of the partially molten upper-mantle deformation in the diffusion creep regime. *Journal of Geophysical Research—Solid Earth* **100**(B2), 1981–2001.

Holtzman, B. K., Groebner, N. J., Zimmerman, M. E., Ginsberg, S. B. & Köhlstedt, D. L. (2003). Stress-driven melt segregation in partially molten rocks. *Geochemistry, Geophysics, Geosystems* **4**, 8607.

Huismans, R. S. & Beaumont, C. (2007). Roles of lithospheric strain softening and heterogeneity in determining the geometry of rifts and continental margins. In: Karner, G. D., Manatschal, G. & Pinheiro, L. M. (eds) *Imaging, Mapping and Modelling Continental Lithosphere Extension and Breakup. Geological Society, London, Special Publications* **282**, 111–138.

Janots, E., Negro, F., Brunet, F., Goffé, B., Engi, M. & Bouybaouène, M. L. (2006). Evolution of the REE mineralogy in HP–LT metapelites of the Sebtide complex, Rif, Morocco: Monazite stability and geochronology. *Lithos* **87**, 214–234.

Jousselin, D., Nicolas, A. & Boudier, F. (1998). Detailed mapping of a mantle diapir below a paleo-spreading center in the Oman ophiolite. *Journal of Geophysical Research* **103**, 153–170.

Jung, H., Katayama, I., Jiang, Z., Hiraga, T. & Karato, S. (2006). Effect of water and stress on the lattice-preferred orientation of olivine. *Tectonophysics* **421**, 1–22.

Kaczmarek, M.-A. & Tommasi, A. (2011). Anatomy of an extensional shear zone in the mantle (Lanzo massif, Italy). *Geochemistry, Geophysics Geosystems* **12**, Q0AG06, doi:10.1029/2011GC003627.

Kendall, J. M., Stuart, G. W., Ebinger, C. J., Bastow, I. D. & Keir, D. (2005). Magma-assisted rifting in Ethiopia. *Nature* **433**, 146–148.

Kelemen, P. B., Dick, H. J. B. & Quick, J. E. (1992). Formation of harzburgite by pervasive melt/rock reactions in the upper mantle. *Nature* **358**, 635–641.

Kornprobst, J. (1969). Le massif ultrabasique des Beni Bouchera (Rif Interne, Maroc): Etude des péridotites de haute température et de haute pression, et des pyroxénolites, à grenat ou sans grenat, qui leur sont associées. *Contributions to Mineralogy and Petrology* **23**, 283–322.

Kornprobst, J. (1970). Les péridotites et les pyroxénolites du massif ultrabasique des Beni Bouchera: une étude expérimentale entre 1100 et 1550°C, sous 15 à 30 kilobars de pression sèche. *Contributions to Mineralogy and Petrology* **29**, 290–309.

Kornprobst, J. (1974). Contribution a l'etude pétrographique et structurale de la zone interne du Rif (Maroc septentrional [petrography and structure of the Rif inner area, northern Morocco]. *Notes et Mémoires du Service Géologique, Rabat* **251**, 1–256.

Kornprobst, J., Piboule, M., Roden, M. & Tabit, A. (1990). Corundum-bearing garnet clinopyroxenites at Beni Bousera (Morocco): original plagioclase-rich gabbros recrystallized at depth within the mantle? *Journal of Petrology* **31**, 717–745.

Kumar, N., Reisberg, L. & Zindler, A. (1996). A major and trace element and strontium, neodymium, and osmium isotopic study of a thick pyroxenite layer from the Beni Bousera ultramafic complex of northern Morocco. *Geochimica et Cosmochimica Acta* **60**, 1429–1444.

Kushiro, I., Syono, Y. & Akimoto, S. (1968). Melting of a peridotite nodule at high pressures and high water pressures. *Journal of Geophysical Research* **73**, 6023–6029.

Lavier, L. & Manatschal, G. (2006). A mechanism to thin the continental lithosphere at magma-poor margins. *Nature* **440**, 324–329.

Lenoir, X., Garrido, C. J., Bodinier, J. L., Dautria, J. M. & Gervilla, F. (2001). The recrystallization front of the Ronda peridotite: Evidence for melting and thermal erosion of subcontinental lithospheric mantle beneath the Alboran basin. *Journal of Petrology* **42**, 141–158.

Le Roux, V., Bodinier, J. L., Tommasi, A., Alard, O., Dautria, J. M., Vauchez, A. & Riches, A. (2007). The Lherz spinel-lherzolite: refertilized rather than pristine mantle. *Earth and Planetary Science Letters* **259**, 599–612, doi:10.1016/j.epsl.2007.05.026.

Le Roux, V., Tommasi, A. & Vauchez, A. (2008). Feedback between melt percolation and deformation in an exhumed lithosphere–asthenosphere boundary. *Earth and Planetary Science Letters* **274**, 401–413.

Loomis, T. P. (1972). Contact metamorphism of pelitic rock by the Ronda ultramafic intrusion, southern Spain. *Geological Society of America Bulletin* **83**, 2449–2474.

Mainprice, D., Tommasi, A., Couvy, H., Cordier, P. & Frost, D. J. (2005). Pressure sensitivity of olivine slip systems and seismic anisotropy in the Earth's upper mantle. *Nature* **433**, 731–733, doi:10.1038/nature03266.

McKenzie, D. (1978). Some remarks on the development of sedimentary basins. *Earth and Planetary Science Letters* **40**, 25–32.

Michard, A., Goffé, B., Boubaouène, L. & Saddiqi, O. (1997). Hercynian Mesozoic thinning in the Alboran Domain. Metamorphic data from the northern Rif, Morocco. *Terra Nova* **9**, 171–174.

Montel, J.-M., Kornprobst, J. & Vielzeuf, D. (2001). Preservation of old U–Th–Pb ages in shielded monazite: example from the Beni Bousera Hercynian kinzigites (Morocco). *Journal of Metamorphic Geology* **18**, 335–342.

Morales, L. F. G. & Tommasi, A. (2011). Composition, textures, seismic and thermal anisotropies of xenoliths from a thin and hot lithospheric mantle (Summit Lake, southern Canadian Cordillera). *Tectonophysics* **507**, 1–15.

Negro, F. (2005). Exhumation des roches métamorphiques du Domaine d'Alboran: étude de la chaîne rifaine (Maroc) et corrélation avec les Cordillères bétiques (Espagne). Ph.D. Thesis, Ecole Normale Supérieure, Paris.

Negro, F., Beyssac, O., Goffé, B., Saddiqi, O. & Bouybaouène, M. L. (2006). Thermal structure of the Alboran Domain in the Rif (northern Morocco) and the Western Betics (southern Spain). Constraints from Raman spectroscopy of carbonaceous material. *Journal of Metamorphic Geology* **24**, 309–327.

Obata, M. (1980). The Ronda peridotite: garnet-, spinel-, and plagioclase-lherzolite facies and the P–T trajectories of a high-temperature mantle intrusion. *Journal of Petrology* **21**, 533–572.

O'Hara, M. J. (1967). Mineral facies in ultramafic rocks. In: Wyllie, P. J. (ed.) *Ultramafic and Related Rocks*. John Wiley, pp. 7–17.

O'Neill, H. S. C. (1981). The transition between spinel lherzolite and garnet lherzolite, and its use as a geobarometer. *Contributions to Mineralogy and Petrology* **77**, 185–194, doi:10.1007/BF00636522.

Pearson, D. G. & Nowell, G. M. (2004). Re–Os and Lu–Hf isotope constraints on the origin and age of pyroxenites from the Beni Bousera peridotite massif: implications for mixed peridotite-pyroxenite mantle sources. *Journal of Petrology* **45**, 439–455, doi:10.1093/petrology/egg102.

Pearson, D. G., Davies, G. R., Nixon, P. H. & Milledge, H. J. (1989). Graphitized diamonds from a peridotite massif in Morocco and implications for anomalous diamond occurrences. *Nature* **338**, 60–62.

Pearson, D. G., Davies, G. R., Nixon, P. H., Greenwood, P. B. & Mattey, D. P. (1991). Oxygen isotope evidence for the origin of pyroxenites in the Beni Bousera peridotite massif, north Morocco: derivation from subducted oceanic lithosphere. *Earth and Planetary Science Letters* **102**, 289–301.

Pearson, D. G., Davies, G. R. & Nixon, P. H. (1993). Geochemical constraints on the petrogenesis of diamond facies pyroxenites from the Beni Bousera peridotite massif, North Morocco. *Journal of Petrology* **34**, 125–172.

Platt, J. P., Anczkiewicz, R., Soto, J. I., Kelley, S. P. & Thirlwall, M. (2006). Early Miocene continental subduction and rapid exhumation in the western Mediterranean. *Geology* **34**, 981–984.

Précigout, J., Gueydan, F., Gapais, D., Garrido, C. J. & Essaifi, A. (2007). Strain localisation in the subcontinental mantle: a ductile alternative to the brittle mantle. *Tectonophysics* **445**, 318–336.

Raterron, P., Amiguet, E., Chen, J., Li, L. & Cordier, P. (2009). Experimental deformation of olivine single crystals at mantle pressure and temperature. *Physics of the Earth and Planetary Interiors* **172**, 74–83.

Reuber, I., Michard, A., Chalouan, A., Juteau, T. & Jermoumi, B. (1982). Structure and emplacement of the Alpine-type peridotites from Beni Bousera, Rif, Morocco: A polyphase tectonic interpretation. *Tectonophysics* **82**, 231–251.

Rolf, T. & Tackley, P. J. (2011). Focussing of stress by continents in 3D spherical mantle convection with self-consistent plate tectonics. *Geophysical Research Letters* **38**, L18301, doi:10.1029/2011GL048677.

Rossetti, F., Theye, T., Lucci, F., Bouybaouène, M., Dini, A., Gerdes, A., Philips, D. & Cozzupoli, D. (2010). Timing and modes of granite magmatism in the core of the Alboran Domain, Rif chain, northern Morocco. Implications for the Alpine evolution of the western Mediterranean. *Tectonics* **29**, 2017.

Saddiqi, O. (1995). Exhumation des roches profondes, péridotites et roches métamorphiques HP–BT dans deux transects de la chaîne alpine: Arc de Gibraltar et Montagnes d'Oman. Unpublished PhD thesis, Université Hassan II, Casablanca.

Saddiqi, O., Reuber, I. & Michard, A. (1988). Sur la tectonique de dénudation du manteau infracontinental dans les Beni Bousera, Rif septentrional, Maroc. *Comptes Rendus de l'Académie des Sciences, Série II* **307**, 657–662.

Saddiqi, O., Feinberg, H., El Azzab, D. & Michard, A. (1995). Paléomagnétisme des péridotites des Beni Bousera (Rif interne, Maroc): conséquences pour l'évolution miocène de l'Arc de Gibraltar. Comptes rendus de l'Académie des sciences. Série 2. *Sciences de la terre et des planètes* **321**, 361–368.

Sandvol, E., Ni, J., Ozalaybey, S. & Schlue, J. (1992). Shear-wave splitting in the Rio Grande Rift. *Geophysical Research Letters* **19**, 2337–2340.

Soustelle, V., Tommasi, A., Bodinier, J. L., Vauchez, A. & Garrido, C. J. M. (2009). Deformation and reactive melt transport in the

mantle lithosphere above a partial melting domain (Ronda peridotite massif, Spain). *Journal of Petrology* **50**, 1235–1266.

Sue, C., Thouvenot, F., Fréchet, J. & Tricart, P. (1999). Widespread extension in the core of the Western Alps revealed by earthquake analysis. *Journal of Geophysical Research* **104**, 611–622.

Sundberg, M. & Cooper, R. (2008). Crystallographic preferred orientation produced by diffusional creep of harzburgite: Effects of chemical interactions among phases during plastic flow. *Journal of Geophysical Research* **113**, B12208, doi:10.1029/2008JB005618.

Tabit, A., Kornprobst, J. & Woodland, A. B. (1997). The garnet peridotites of the Beni Bousera massif (Morocco): Tectonic mixing and iron–magnesium interdiffusion. *Comptes Rendus de l'Académie des Sciences* **325**, 665–670.

Takahashi, E. & Kushiro, I. (1983). Melting of a dry peridotite at high pressures and basalt magma genesis. *American Mineralogist* **68**, 859–879.

Targuisti, K. (1994). Petrología y geoquímica de los macizos ultramaficos de Ojen (Andalucía) y de Béni Bousera (Rif Septentrional, Marruecos). Unpublished PhD thesis, University of Granada.

Tikoff, B., Russo, R., Teyssier, C. & Tommasi, A. (2004). Mantle-driven deformation of orogenic zones and clutch tectonics. In: Grocott, J., McCaffrey, K., Taylor, G. & Tikoff, B. (eds) *Vertical and Horizontal Decoupling in the Lithosphere. Geological Society, London, Special Publications* **227**, 41–64.

Tommasi, A., Tikoff, B. & Vauchez, A. (1999). Upper mantle tectonics: three-dimensional deformation, olivine crystallographic fabrics and seismic properties. *Earth and Planetary Science Letters* **168**, 173–186.

Tommasi, A., Mainprice, D., Canova, G. & Chastel, Y. (2000). Viscoplastic self-consistent and equilibrium-based modeling of olivine lattice preferred orientations: Implications for the upper mantle seismic anisotropy. *Journal of Geophysical Research* **105**(B4), 7893–7908.

Tommasi, A., Gibert, B., Seipold, U. & Mainprice, D. (2001). Anisotropy of thermal diffusivity in the upper mantle. *Nature* **411**, 783–786.

Tommasi, A., Godard, M., Coromina, G., Dautria, J.-M. & Barsczus, H. (2004). Seismic anisotropy and compositionally induced velocity anomalies in the lithosphere above mantle plumes: a petrological and microstructural study of mantle xenoliths from French Polynesia. *Earth and Planetary Science Letters* **227**, 539–556.

Tommasi, A., Vauchez, A. & Ionov, D. A. (2008). Deformation, static recrystallization, and reactive melt transport in shallow subcontinental mantle xenoliths (Tok Cenozoic volcanic field, SE Siberia). *Earth and Planetary Science Letters* **272**, 65–77, doi:10.1016/j.epsl.2008.04.020.

Tommasi, A., Knoll, M., Vauchez, A., Signorelli, J., Thoraval, C. & Logé, R. (2009). Structural reactivation in plate tectonics controlled by olivine crystal anisotropy. *Nature Geoscience* **2**, 423–427.

Tubía, J. M. (1994). The Ronda peridotites (Los Reales nappe): an example of the relationship between lithospheric thickening by oblique tectonics and late extensional deformation within the Betic Cordillera (Spain). *Tectonophysics* **238**, 381–398.

Tubía, J. M., Cuevas, J. & Esteban, J. J. (2004). Tectonic evidence in the Ronda peridotites, Spain, for mantle diapirism related to delamination. *Geology* **32**, 941–944.

Ulrich, S. & Mainprice, D. (2005). Does cation ordering in omphacites influence the development of lattice-preferred orientation? *Journal of Structural Geology* **27**, 419–431.

Van der Wal, D. & Bodinier, J. L. (1996). Origin of the recrystallization front in the Ronda peridotite by km-scale pervasive porous melt flow. *Contributions to Mineralogy and Petrology* **122**, 387–405.

Van der Wal, D. & Vissers, R. L. M. (1993). Uplift and emplacement of upper mantle rocks in the western Mediterranean. *Geology* **21**, 1119–1122.

Van der Wal, D. & Vissers, R. L. M. (1996). Structural petrology of the Ronda peridotite, SW Spain: Deformation history. *Journal of Petrology* **37**, 23–43.

Vauchez, A. & Garrido, C. J. (2001). Seismic properties of an asthenospherized lithospheric mantle: constraints from lattice preferred orientations in peridotite from the Ronda Massif. *Earth and Planetary Science Letters* **192**, 235–249.

Vauchez, A., Tommasi, A., Barruol, G. & Maumus, J. (2000). Upper mantle deformation and seismic anisotropy in continental rifts. *Physics and Chemistry of the Earth (A)* **25**, 111–117.

Vauchez, A., Tommasi, A. & Mainprice, D. (2012). Faults (shear zones) in the Earth's mantle. *Tectonophysics* **558–559**, 1–27, doi:10.1016/j.tecto.2012.06.006.

Vollmer, F. W. (1990). An application of eigenvalue methods to structural domain analysis. *Geological Society of America Bulletin* **102**, 786–791.

Webb, S. A. C. & Wood, B. J. (1986). Spinel–pyroxene–garnet relationships and their dependence on Cr/Al ratio. *Contributions to Mineralogy and Petrology* **92**, 471–480, doi:10.1007/BF00374429.

Wernicke, B. (1981). Low angle normal faults in Basin and Range province. Nappe tectonics in an extending orogen. *Nature* **291**, 645–648.

Wernicke, B. (1985). Uniform-sense normal simple shear of the continental lithosphere. *Canadian Journal of Earth Sciences* **22**, 108–125.

Zhang, S. & Karato, S. (1995). Lattice preferred orientation of olivine aggregates in simple shear. *Nature* **375**, 774–777.